Supporting Information

Au/UiO-66-Zr nanohybrids: Boosting yield rates of electrochemical ammonia synthesis at sacrifice of Faradaic efficiencies

Xiaoyu Qian [a]†, Lu Ding [a]†, Yanling Zhao [a], Zhichun Li [a], Yuanxiu Liao [a], Jiabin Tan [b] and Xiaobo He [a]*

[a] Jiangsu Key Laboratory of Advanced Catalytic Materials and Technology, School of Petrochemical Engineering, Changzhou University, Changzhou 213164, P.R. China

[b] College of Chemical Engineering, Beijing University of Chemical Technology, Beijing 100029, P.R. China

*Corresponding author

Tel.: +86-519-86330253

E-mail: hexiaobo@cczu.edu.cn

† These authors contributed equally.

Supporting Figures.

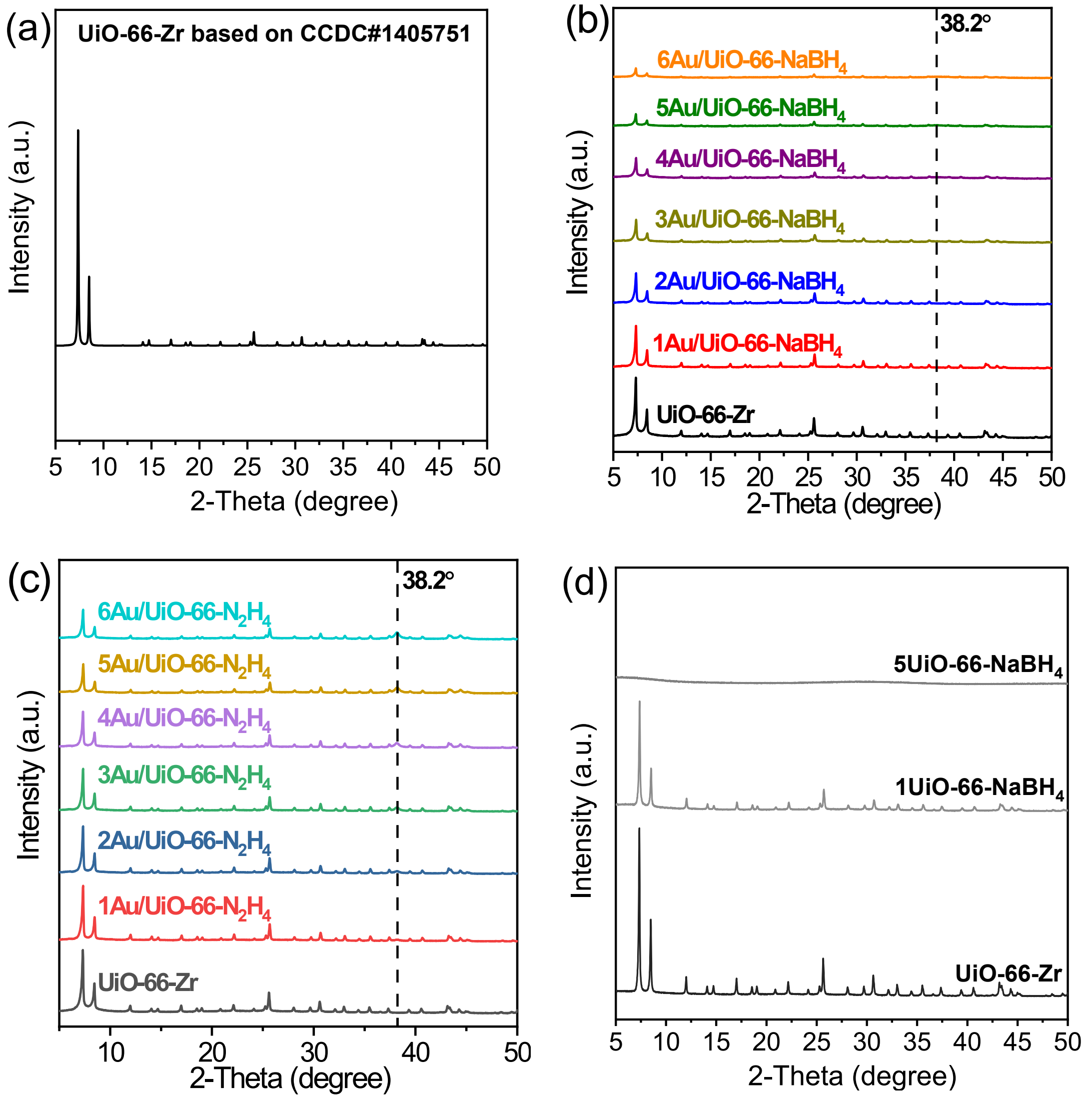

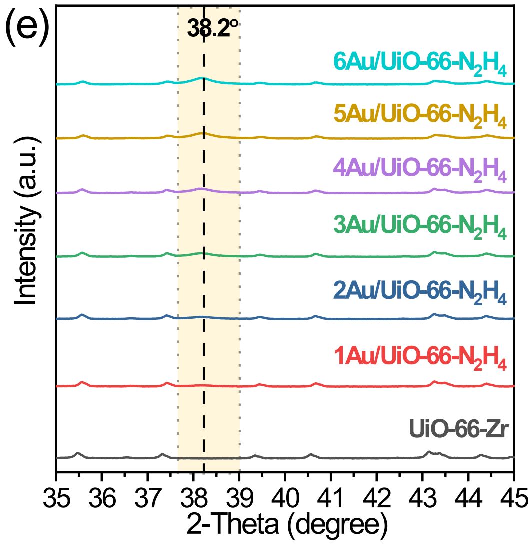

Fig. S1. XRD patterns: (a) Simulated one of UiO-66-Zr on the basis of the structure of CCDC#1405751; (b) The prepared pristine UiO-66-Zr and *x*Au/UiO-66-$NaBH_4$; (c) *x*Au/UiO-66-N_2H_4; (d) The pristine UiO-66-Zr, 1UiO-66-$NaBH_4$ and 5UiO-66-$NaBH_4$, in which 1UiO-66-$NaBH_4$ and 5UiO-66-$NaBH_4$ are the pristine UiO-66-Zr treated by 1 mL and 5 mL of 0.5 M $NaBH_4$ solution (the solvent was a mixture of anhydrous ethanol and ultrapure water with a volume ratio of 1:1), respectively; (e) Zoomed in ones of the pristine UiO-66-Zr and *x*Au/UiO-66-N_2H_4.

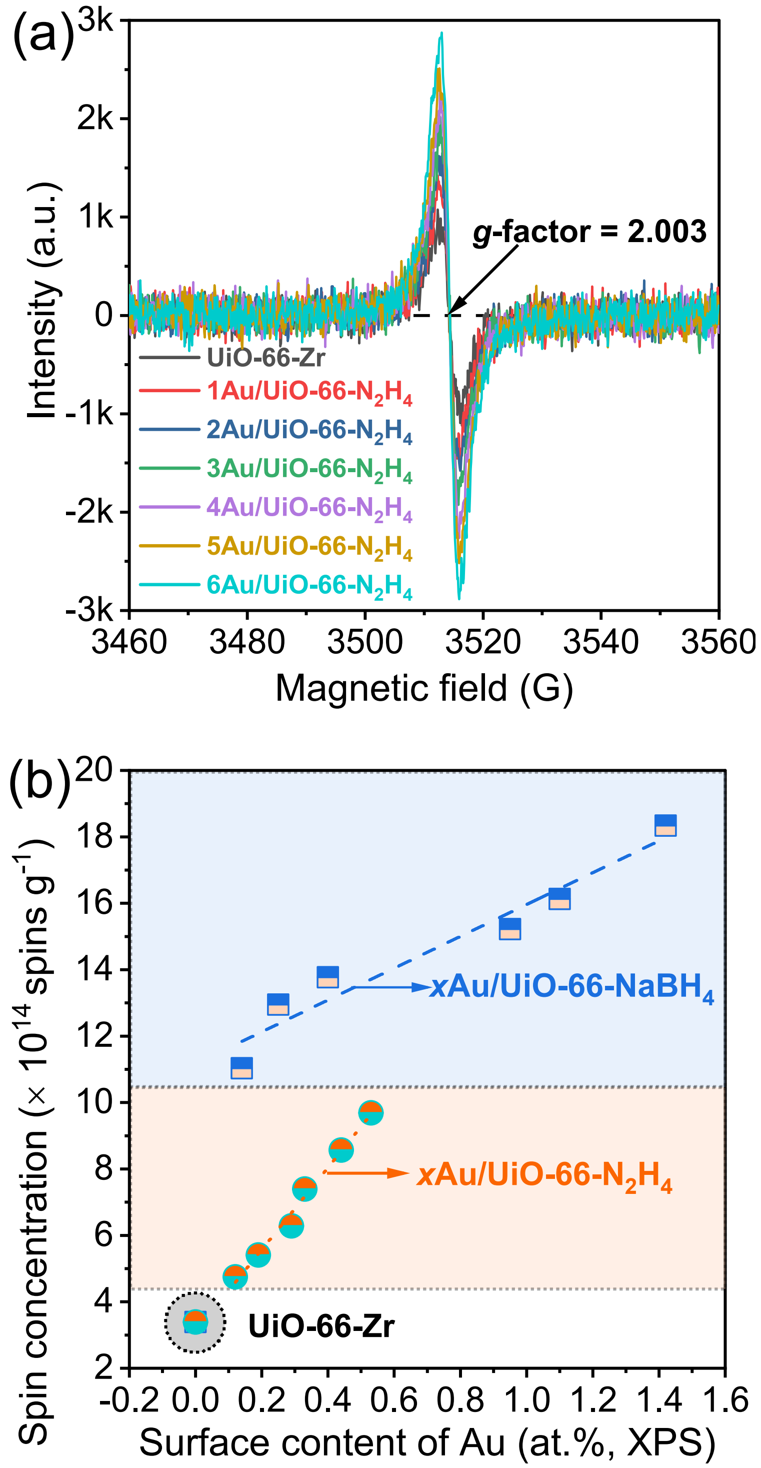

Fig. S2. (a) ESR of UiO-66-Zr and *x*Au/UiO-66-N_2H_4; (b) Relationships between surface contents of Au and spin concentrations for both *x*Au/UiO-66-$NaBH_4$ and *x*Au/UiO-66-N_2H_4.

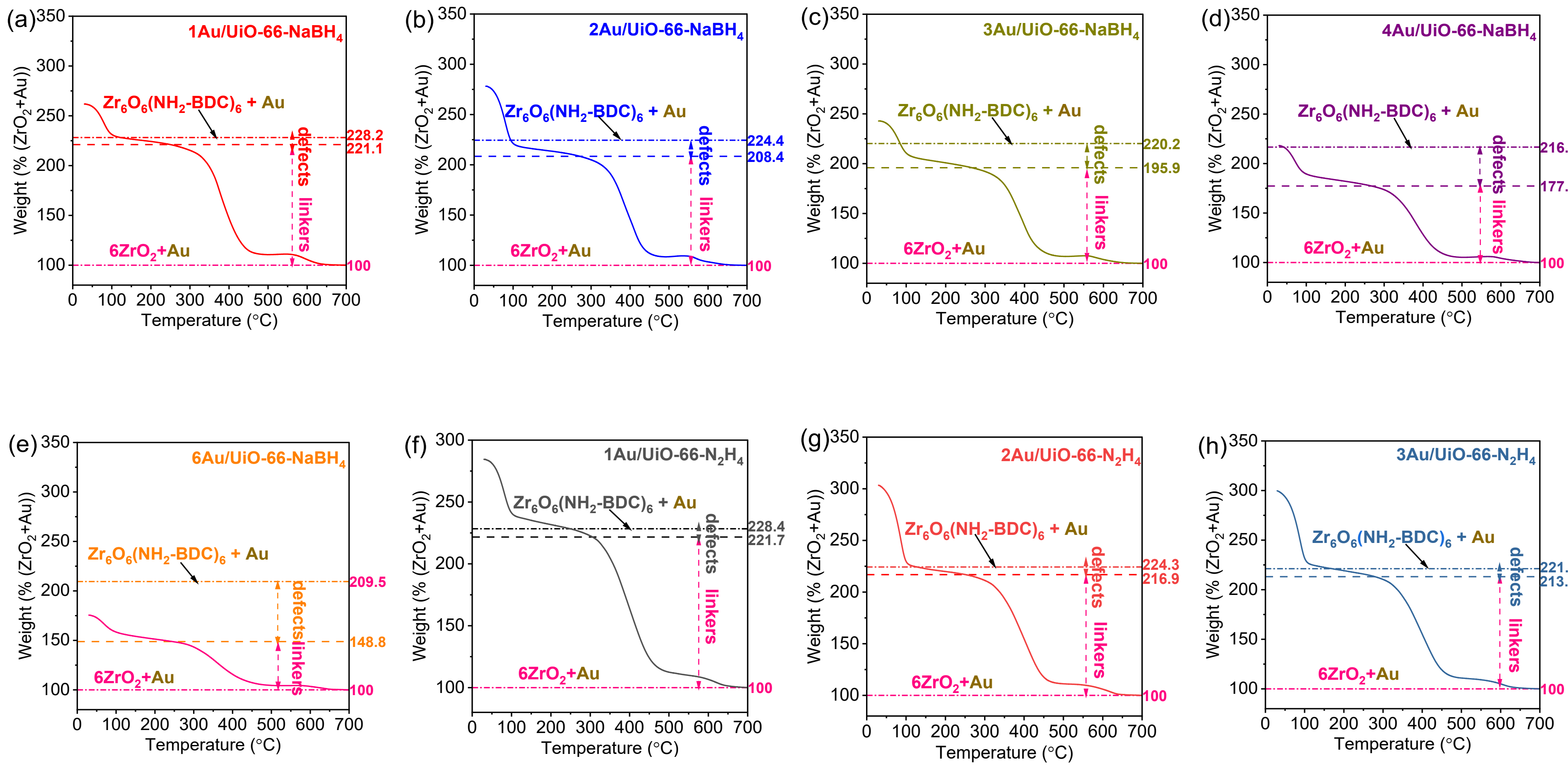

(a) 1Au/UiO-66-NaBH$_4$
Zr$_6$O$_6$(NH$_2$-BDC)$_6$ + Au
228.2
221.1
defects
linkers
6ZrO$_2$+Au
100
(b) 2Au/UiO-66-NaBH$_4$
Zr$_6$O$_6$(NH$_2$-BDC)$_6$ + Au
224.4
208.4
defects
linkers
6ZrO$_2$+Au
100
(c) 3Au/UiO-66-NaBH$_4$
Zr$_6$O$_6$(NH$_2$-BDC)$_6$ + Au
220.2
195.9
defects
linkers
6ZrO$_2$+Au
100
(d) 4Au/UiO-66-NaBH$_4$
Zr$_6$O$_6$(NH$_2$-BDC)$_6$ + Au
216.6
177.3
defects
linkers
6ZrO$_2$+Au
100
(e) 6Au/UiO-66-NaBH$_4$
Zr$_6$O$_6$(NH$_2$-BDC)$_6$ + Au
209.5
148.8
defects
linkers
6ZrO$_2$+Au
100
(f) 1Au/UiO-66-N$_2$H$_4$
Zr$_6$O$_6$(NH$_2$-BDC)$_6$ + Au
228.4
221.7
defects
linkers
6ZrO$_2$+Au
100
(g) 2Au/UiO-66-N$_2$H$_4$
Zr$_6$O$_6$(NH$_2$-BDC)$_6$ + Au
224.3
216.9
defects
linkers
6ZrO$_2$+Au
100
(h) 3Au/UiO-66-N$_2$H$_4$
Zr$_6$O$_6$(NH$_2$-BDC)$_6$ + Au
221.2
213.1
defects
linkers
6ZrO$_2$+Au
100
Weight (% (ZrO$_2$+Au))
Temperature (°C)

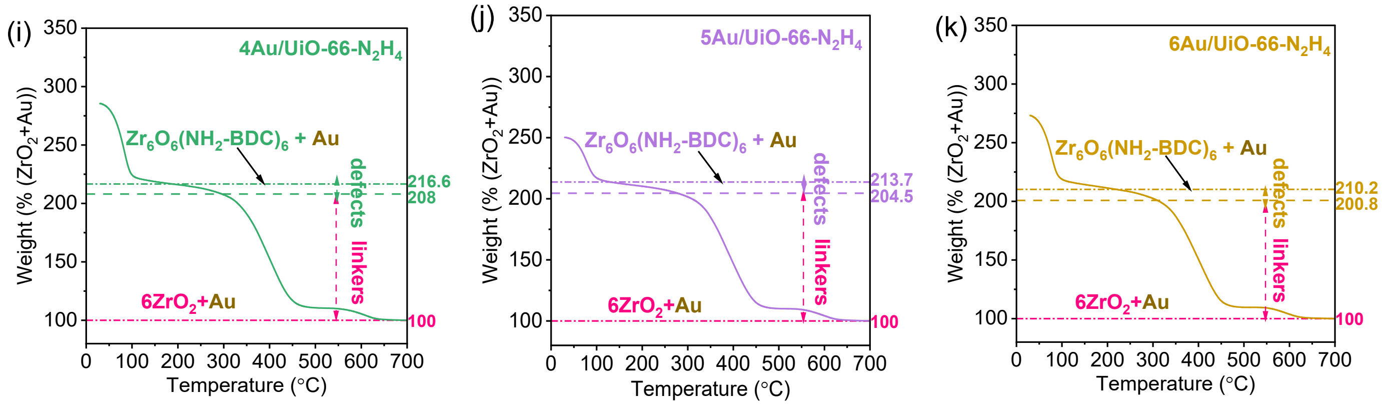

Fig. S3. TG curves in air of *x*Au/UiO-66-$NaBH_4$ (x = 1 (a), 2 (b), 3 (c), 4 (d), and 6 (e)) and *x*Au/UiO-66-N_2H_4 (x = 1 (f), 2 (g), 3 (h), 4 (i), 5 (j), and 6 (k)).

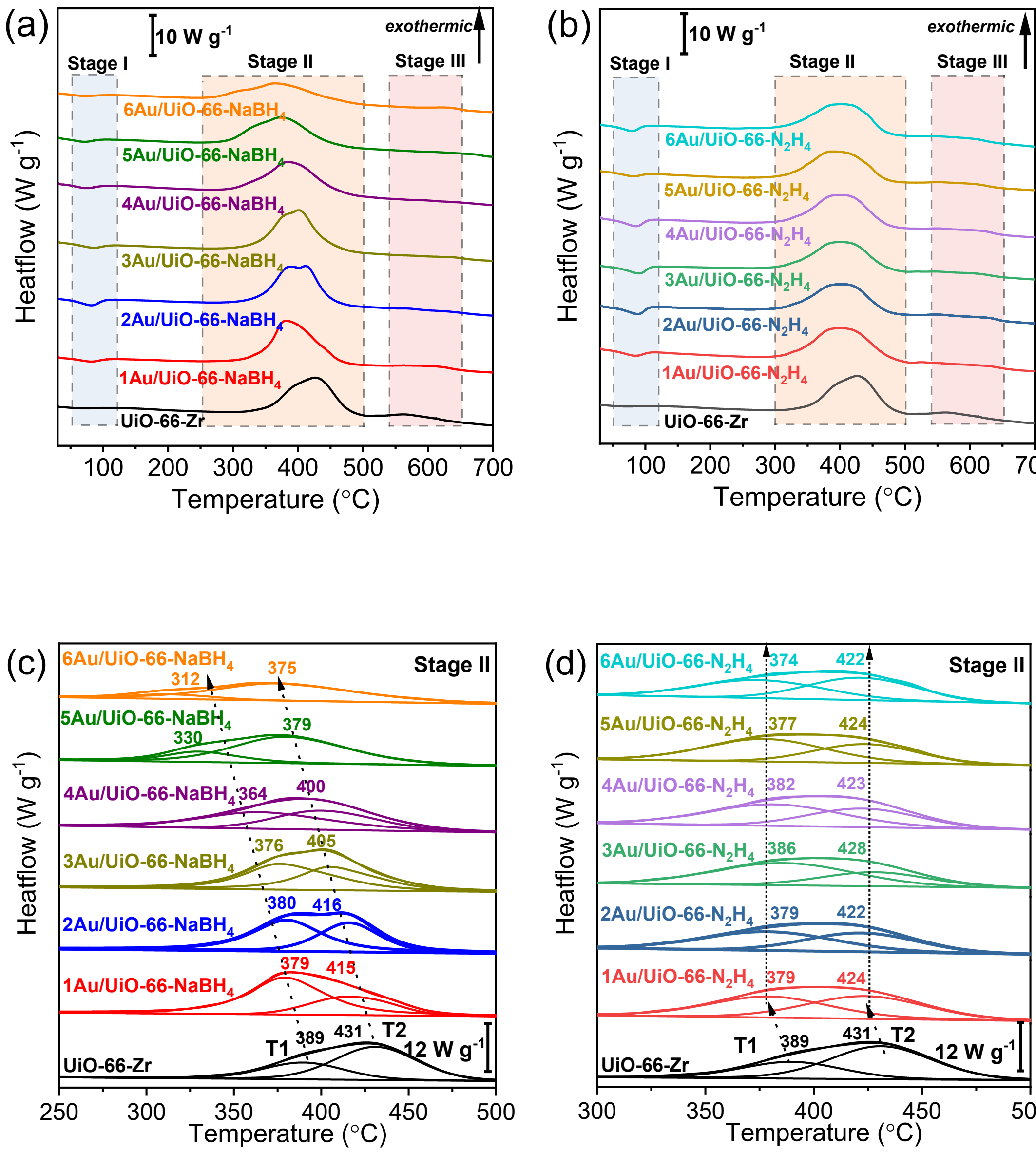

Fig. S4. DSC curves in air: (a) The pristine UiO-66-Zr and *x*Au/UiO-66-$NaBH_4$; (b) The pristine UiO-66-Zr and *x*Au/UiO-66-N_2H_4; (c) Stage II of the pristine UiO-66-Zr and *x*Au/UiO-66-$NaBH_4$; (d) Stage II of the pristine UiO-66-Zr and *x*Au/UiO-66-N_2H_4.

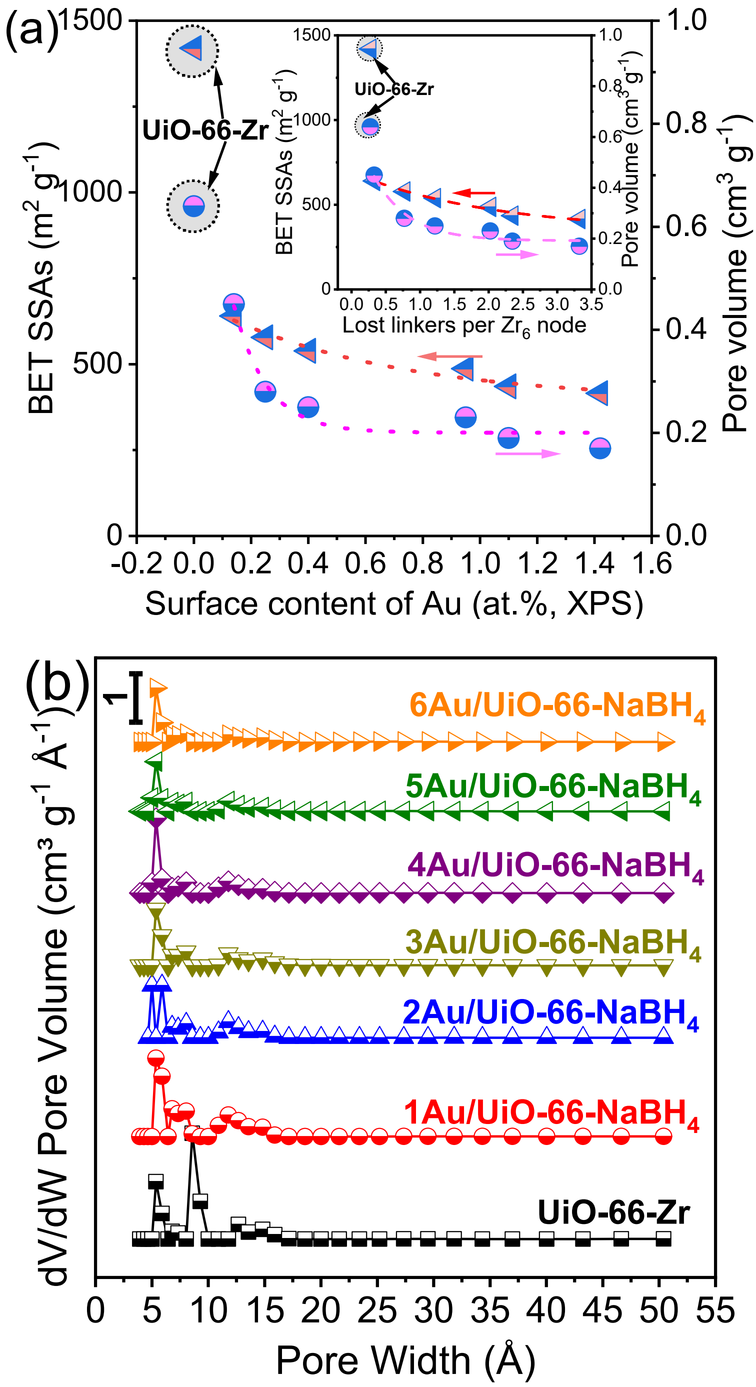

Fig. S5. Porosity for *x*Au/UiO-66-NaBH$_4$: (a) Relationship between surface contents of Au and BET SSAs, and that between surface contents of Au and pore volumes, and the inset shows relationship between lost linkers per Zr$_6$ node and BET SSAs, and that between lost linkers per Zr$_6$ node and pore volumes; (b) Pore size distributions.

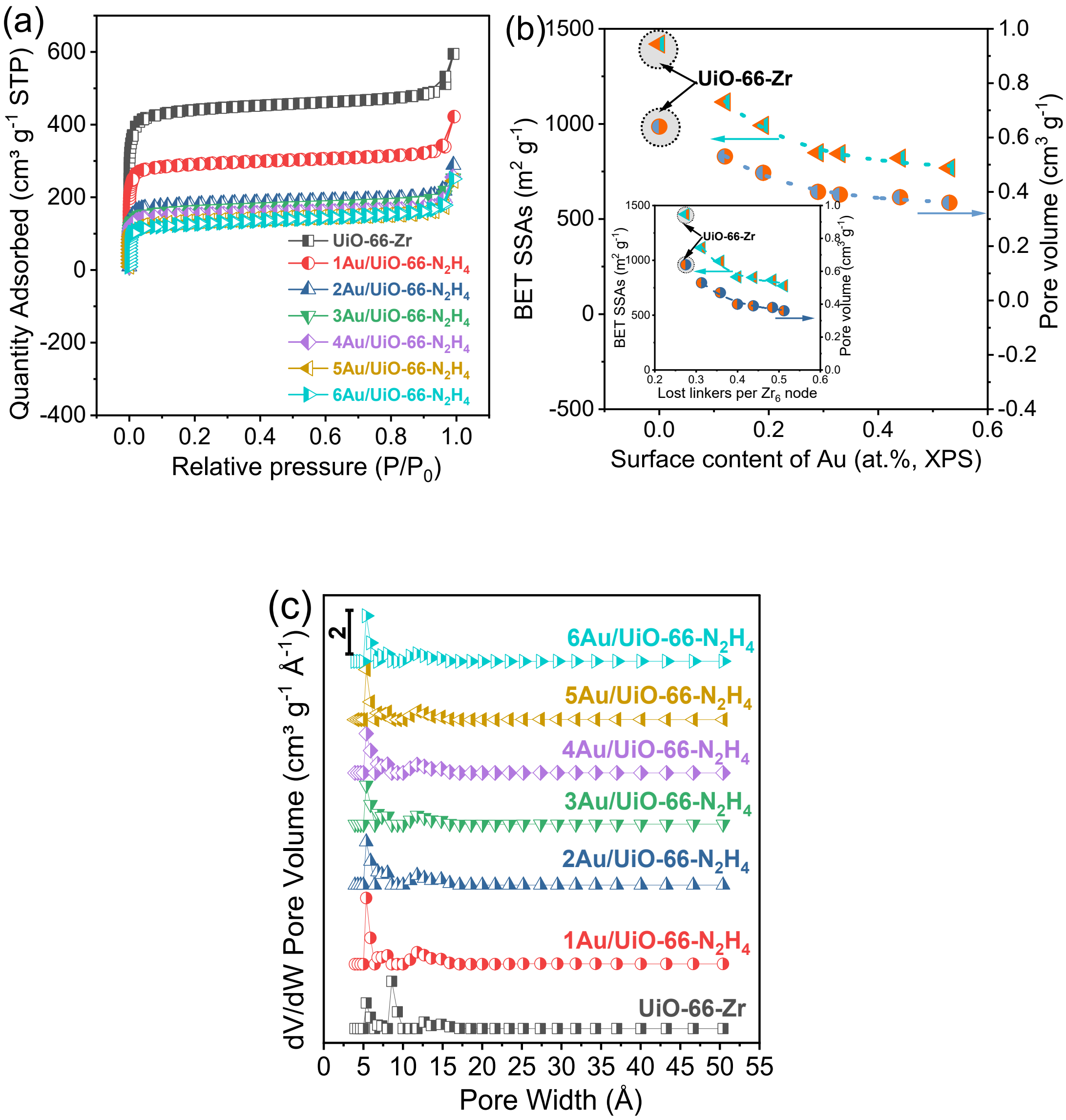

Fig. S6. Porosity for *x*Au/UiO-66-N_2H_4: (a) N_2-sorption isotherms at 77 K of the pristine UiO-66-Zr and *x*Au/UiO-66-N_2H_4; (b) Relationship between surface contents of Au and BET SSAs, and that between surface contents of Au and pore volumes, and the inset shows relationship between lost linkers per Zr_6 node and BET SSAs, and that between lost linkers per Zr_6 node and pore volumes; (c) Pore size distributions.

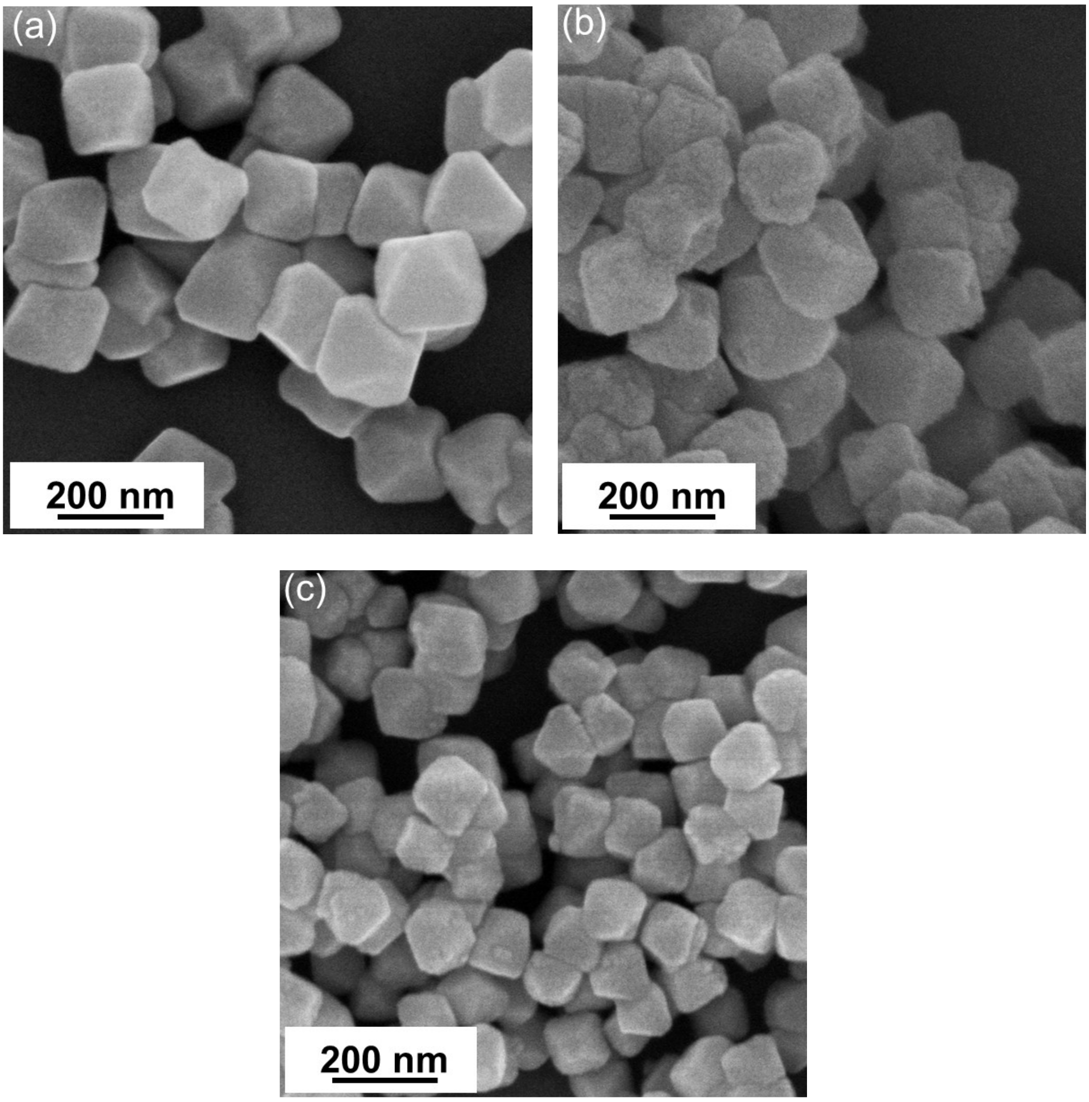

Fig. S7. SEM images: (a) The pristine UiO-66-Zr; (b) 1UiO-66-$NaBH_4$; (c) 5UiO-66-$NaBH_4$.

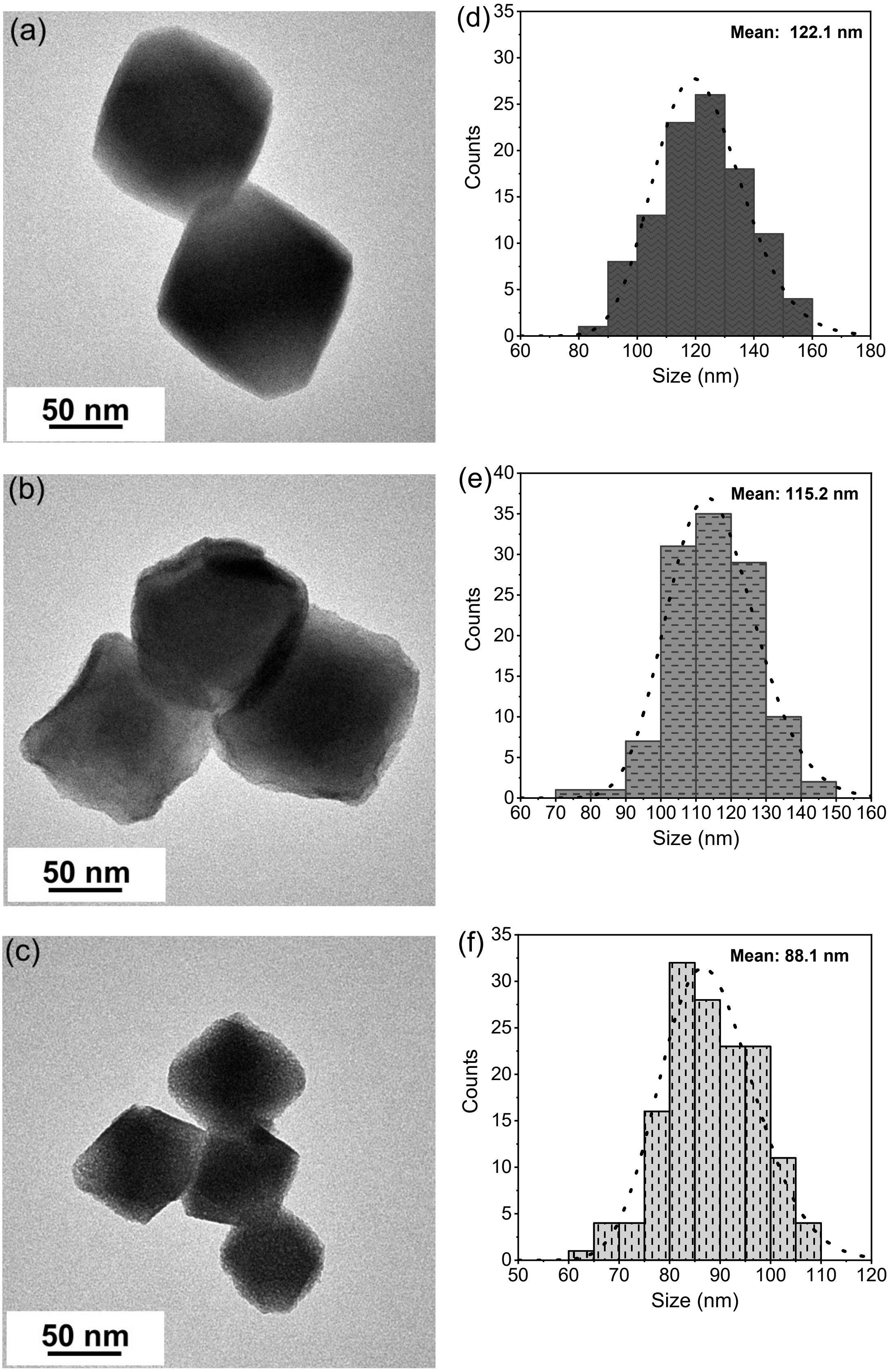

Fig. S8. TEM images and size distributions: (a) The pristine UiO-66-Zr; (b) 1UiO-

66-$NaBH_4$; (c) 5UiO-66-$NaBH_4$; (d) Side length distribution of octahedral pristine UiO-66-Zr nanoparticles; (e) Side length distribution of octahedral 1UiO-66-$NaBH_4$ nanoparticles; (f) Side length distribution of octahedral 5UiO-66-$NaBH_4$ nanoparticles.

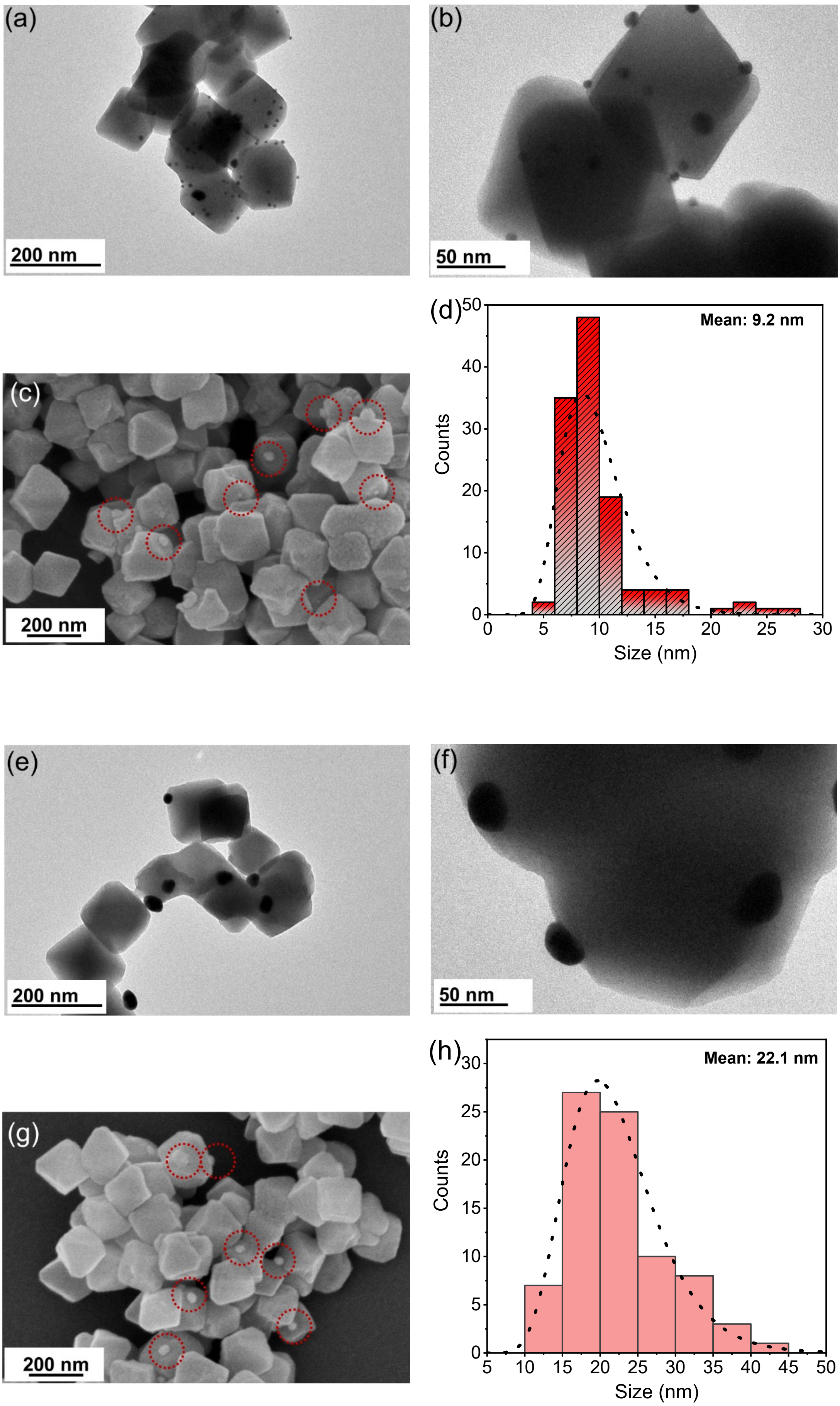
(a)
200 nm
(b)
50 nm
(c)
200 nm
(d)
Mean: 9.2 nm
Counts
Size (nm)
(e)
200 nm
(f)
50 nm
(g)
200 nm
(h)
Mean: 22.1 nm
Counts
Size (nm)

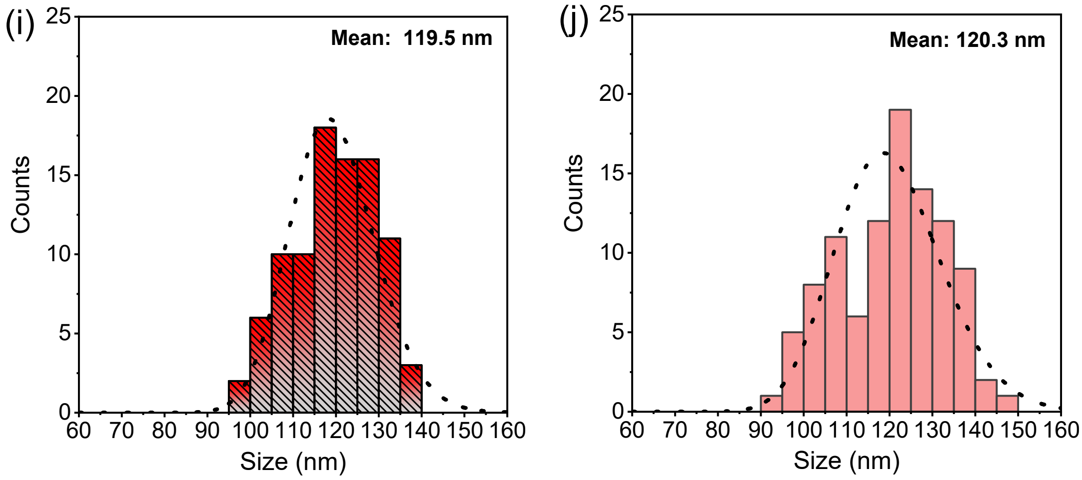

Fig. S9. TEM and SEM images and size distributions of Au and UiO-66-Zr support nanoparticles for other samples: (a) and (b) TEM images of 1Au/UiO-66-$NaBH_4$; (c) SEM image of 1Au/UiO-66-$NaBH_4$, in which some Au nanoparticles are marked by red dotted circles; (d) Corresponding size distributions of Au nanoparticles in 1Au/UiO-66-$NaBH_4$; (e) and (f) TEM images of 1Au/UiO-66-N_2H_4; (g) SEM image of 1Au/UiO-66-N_2H_4, in which some Au nanoparticles are marked by red dotted circles; (h) Corresponding size distributions of Au nanoparticles in 1Au/UiO-66-N_2H_4; (i) Side length distribution of octahedral UiO-66-Zr support nanoparticles in 1Au/UiO-66-$NaBH_4$; (j) Side length distribution of octahedral UiO-66-Zr support nanoparticles in 1Au/UiO-66-N_2H_4.

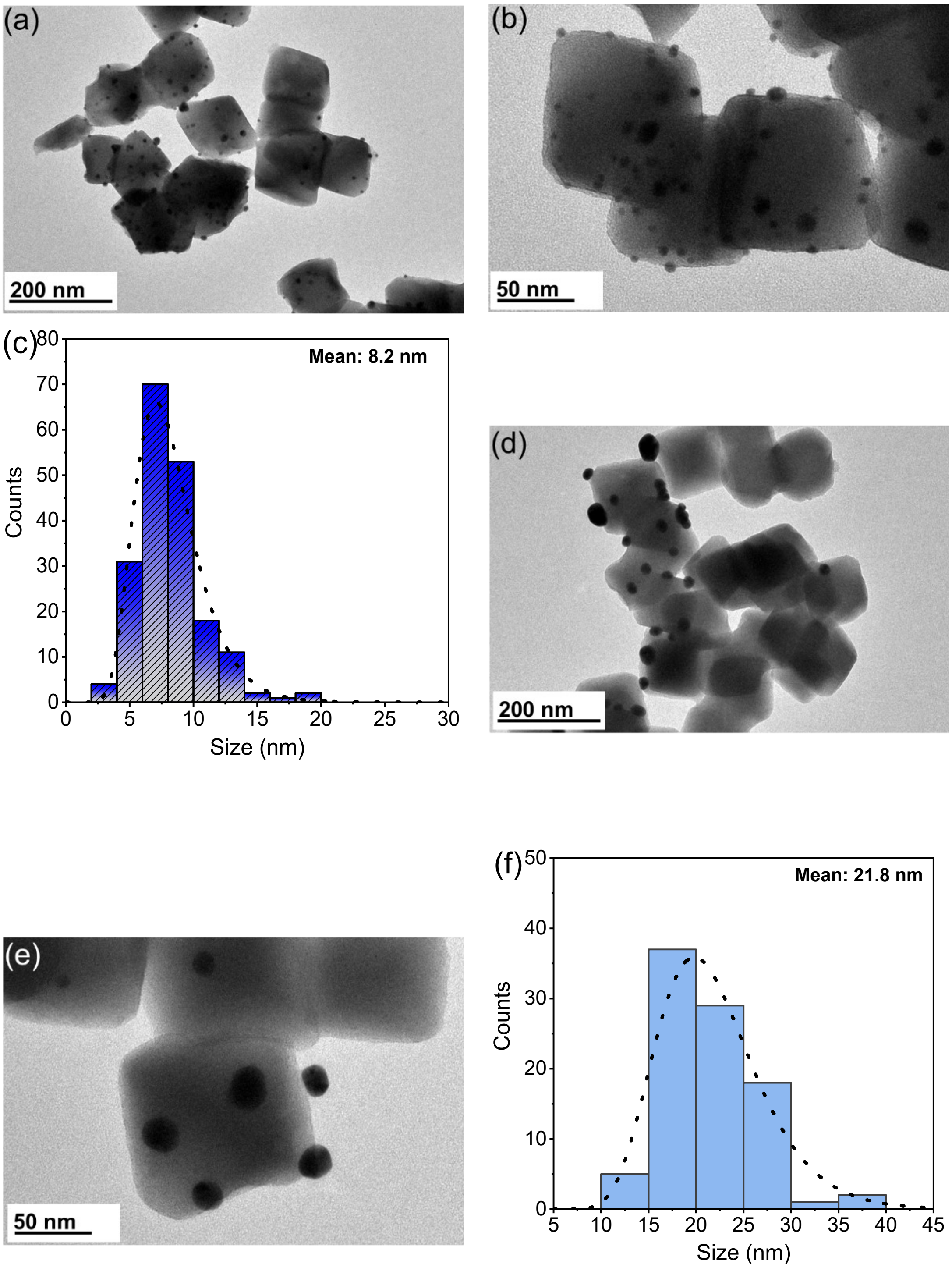
(a)
200 nm
(b)
50 nm
(c)
Mean: 8.2 nm
Counts
Size (nm)
0
5
10
15
20
25
30
0
10
20
30
40
50
60
70
80
(d)
200 nm
(e)
50 nm
(f)
Mean: 21.8 nm
Counts
Size (nm)
5
10
15
20
25
30
35
40
45
0
10
20
30
40
50

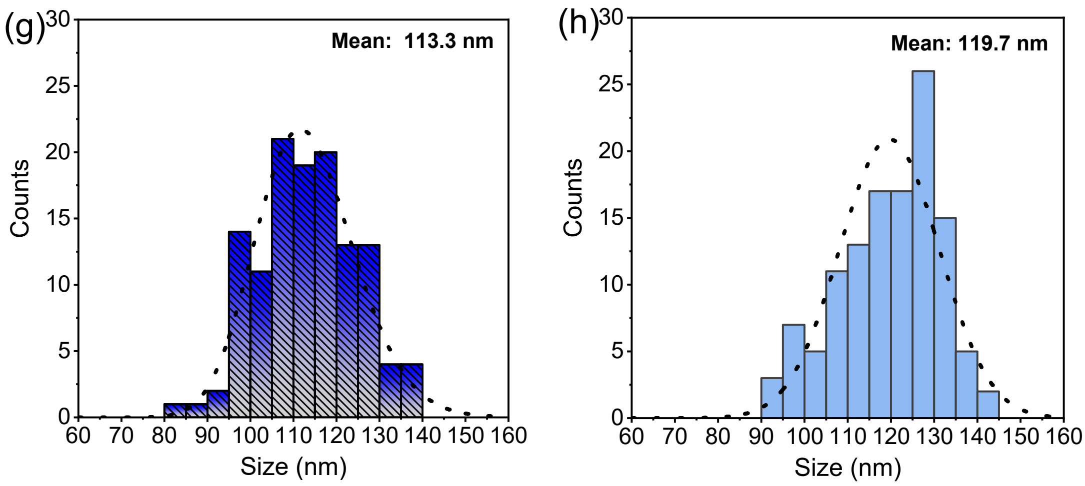

Fig. S10. TEM and SEM images and size distributions of Au and UiO-66-Zr support nanoparticles for other samples: (a) and (b) 2Au/UiO-66-NaBH$_4$; (c) Corresponding size distributions of Au nanoparticles in 2Au/UiO-66-NaBH$_4$; (d) and (e) 2Au/UiO-66-N$_2$H$_4$; (f) Corresponding size distributions of Au nanoparticles in 2Au/UiO-66-N$_2$H$_4$; (g) Side length distribution of octahedral UiO-66-Zr support nanoparticles in 2Au/UiO-66-NaBH$_4$; (h) Side length distribution of octahedral UiO-66-Zr support nanoparticles in 2Au/UiO-66-N$_2$H$_4$.

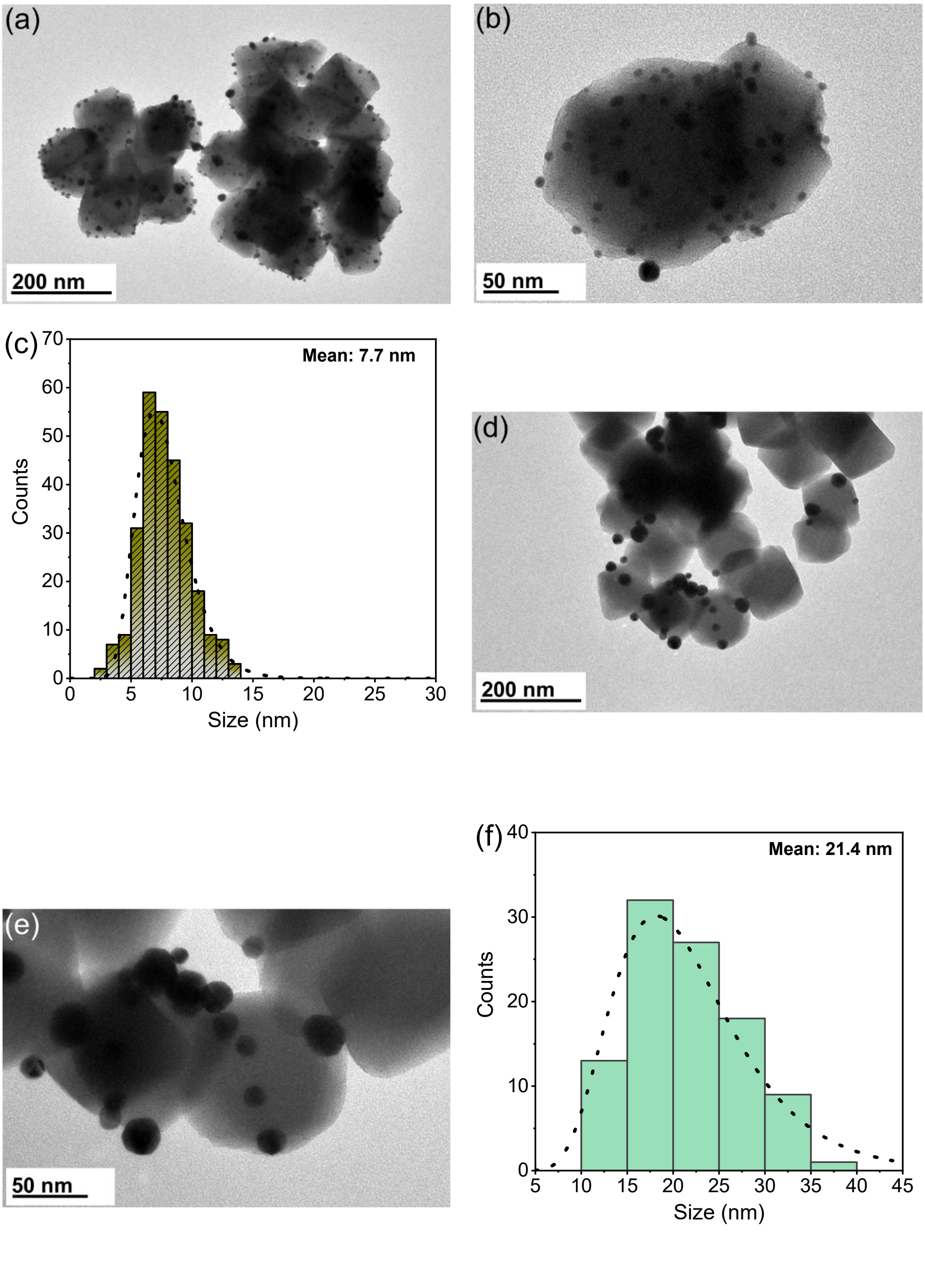
(a)
200 nm
(b)
50 nm
(c)
Mean: 7.7 nm
Counts
0
10
20
30
40
50
60
70
0
5
10
15
20
25
30
Size (nm)
(d)
200 nm
(e)
50 nm
(f)
Mean: 21.4 nm
Counts
0
10
20
30
40
5
10
15
20
25
30
35
40
45
Size (nm)

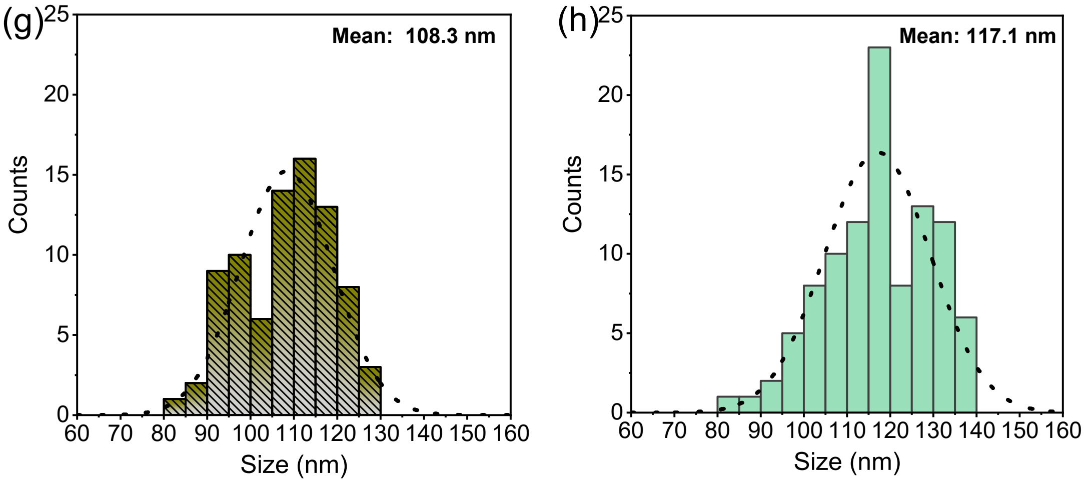

Fig. S11. TEM and SEM images and size distributions of Au and UiO-66-Zr support nanoparticles for other samples: (a) and (b) 3Au/UiO-66-$NaBH_4$; (c) Corresponding size distributions of Au nanoparticles in 3Au/UiO-66-$NaBH_4$; (d) and (e) 3Au/UiO-66-N_2H_4; (f) Corresponding size distributions of Au nanoparticles in 3Au/UiO-66-N_2H_4; (g) Side length distribution of octahedral UiO-66-Zr support nanoparticles in 3Au/UiO-66-$NaBH_4$; (h) Side length distribution of octahedral UiO-66-Zr support nanoparticles in 3Au/UiO-66-N_2H_4.

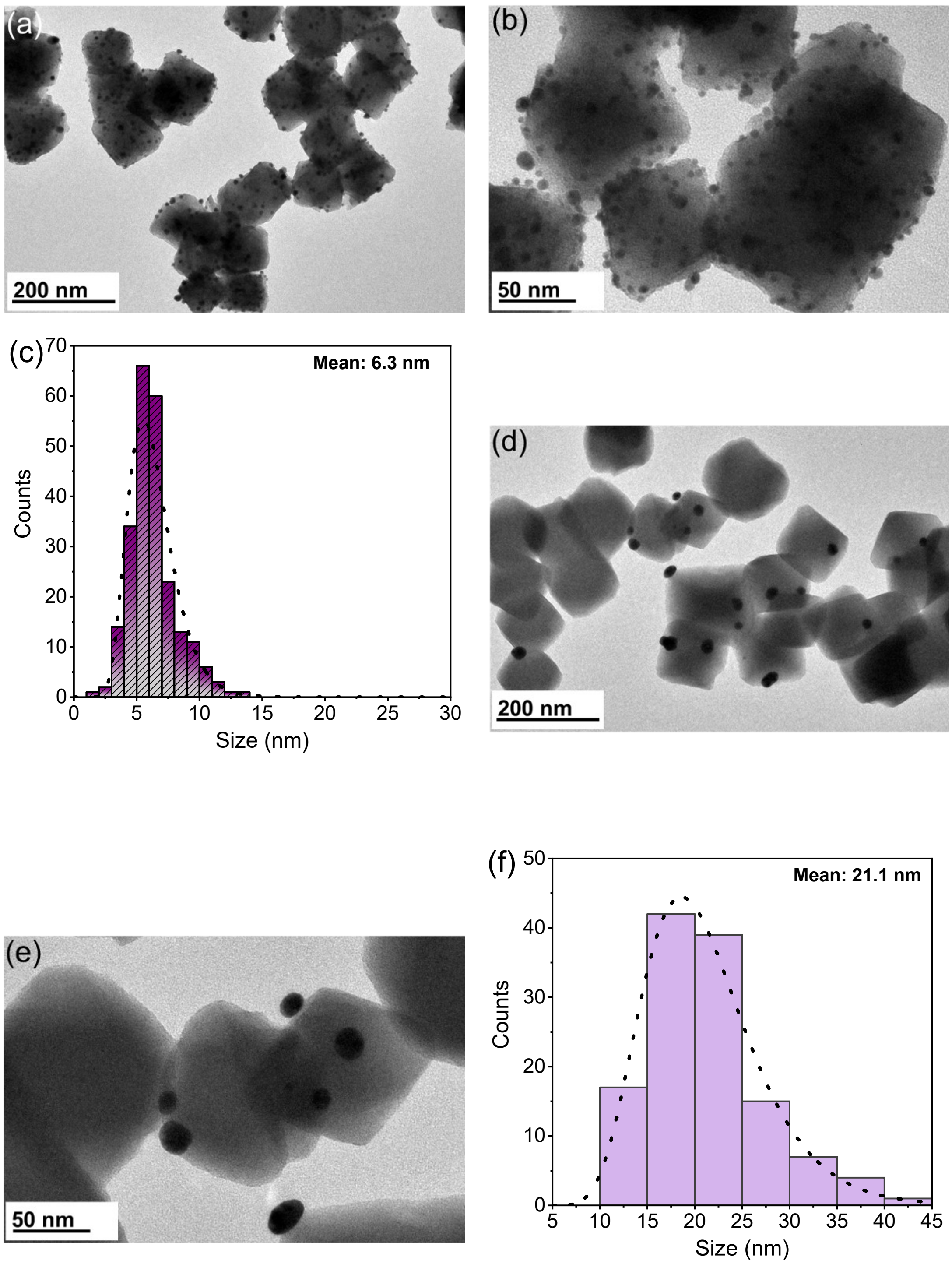
(a)
200 nm
(b)
50 nm
(c)
Mean: 6.3 nm
Counts
Size (nm)
0
10
20
30
40
50
60
70
0
5
10
15
20
25
30
(d)
200 nm
(e)
50 nm
(f)
Mean: 21.1 nm
Counts
Size (nm)
0
10
20
30
40
50
5
10
15
20
25
30
35
40
45

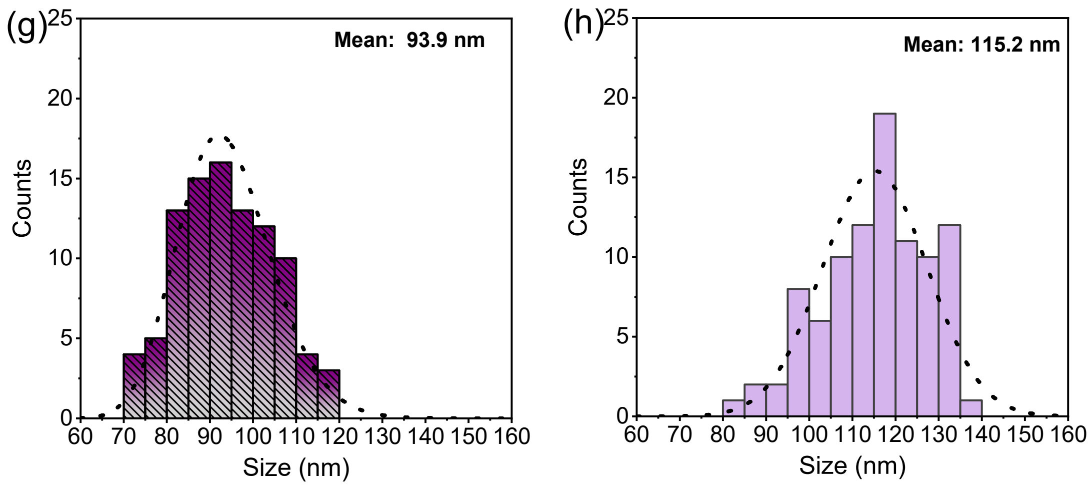

Fig. S12. TEM and SEM images and size distributions of Au and UiO-66-Zr support nanoparticles for other samples: (a) and (b) 4Au/UiO-66-$NaBH_4$; (c) Corresponding size distributions of Au nanoparticles in 4Au/UiO-66-$NaBH_4$; (d) and (e) 4Au/UiO-66-N_2H_4; (f) Corresponding size distributions of Au nanoparticles in 4Au/UiO-66-N_2H_4; (g) Side length distribution of octahedral UiO-66-Zr support nanoparticles in 4Au/UiO-66-$NaBH_4$; (h) Side length distribution of octahedral UiO-66-Zr support nanoparticles in 4Au/UiO-66-N_2H_4.

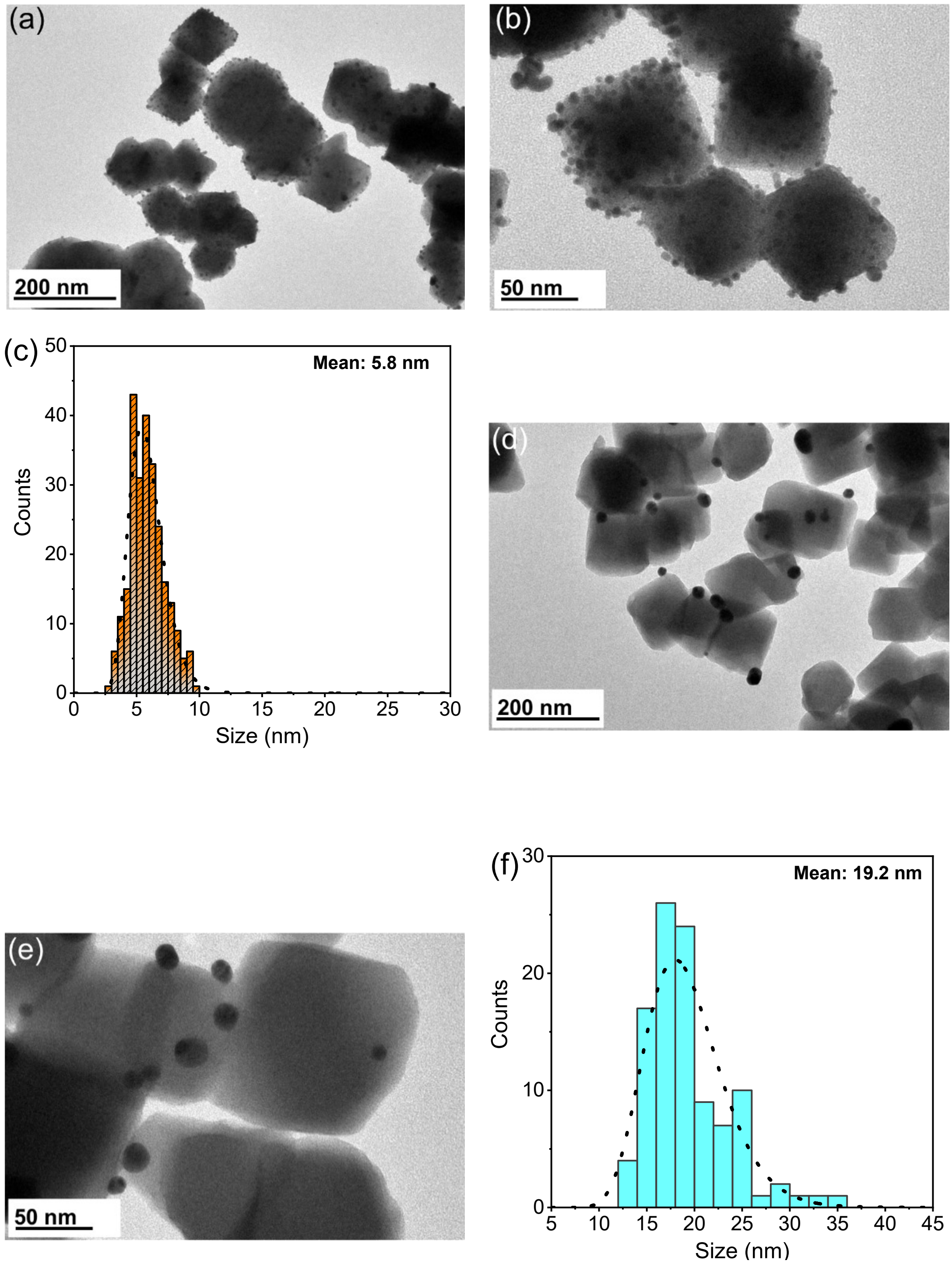
(a)
200 nm
(b)
50 nm
(c)
Mean: 5.8 nm
Counts
Size (nm)
0
5
10
15
20
25
30
40
50
(d)
200 nm
(e)
50 nm
(f)
Mean: 19.2 nm
Counts
Size (nm)
0
5
10
15
20
25
30
35
40
45

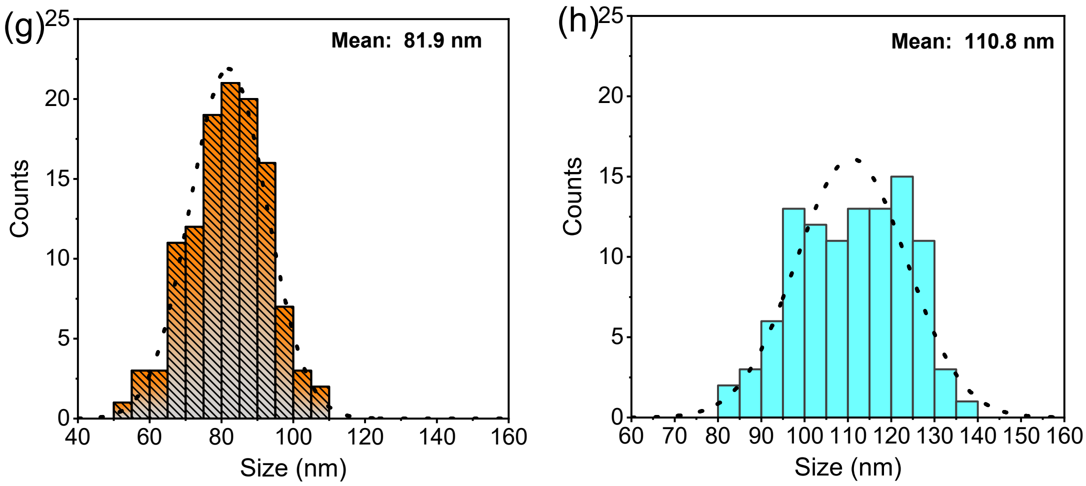

Fig. S13. TEM and SEM images and size distributions of Au and UiO-66-Zr support nanoparticles for other samples: (a) and (b) 6Au/UiO-66-$NaBH_4$; (c) Corresponding size distributions of Au nanoparticles in 6Au/UiO-66-$NaBH_4$; (d) and (e) 6Au/UiO-66-N_2H_4; (f) Corresponding size distributions of Au nanoparticles in 6Au/UiO-66-N_2H_4; (g) Side length distribution of octahedral UiO-66-Zr support nanoparticles in 6Au/UiO-66-$NaBH_4$; (h) Side length distribution of octahedral UiO-66-Zr support nanoparticles in 6Au/UiO-66-N_2H_4.

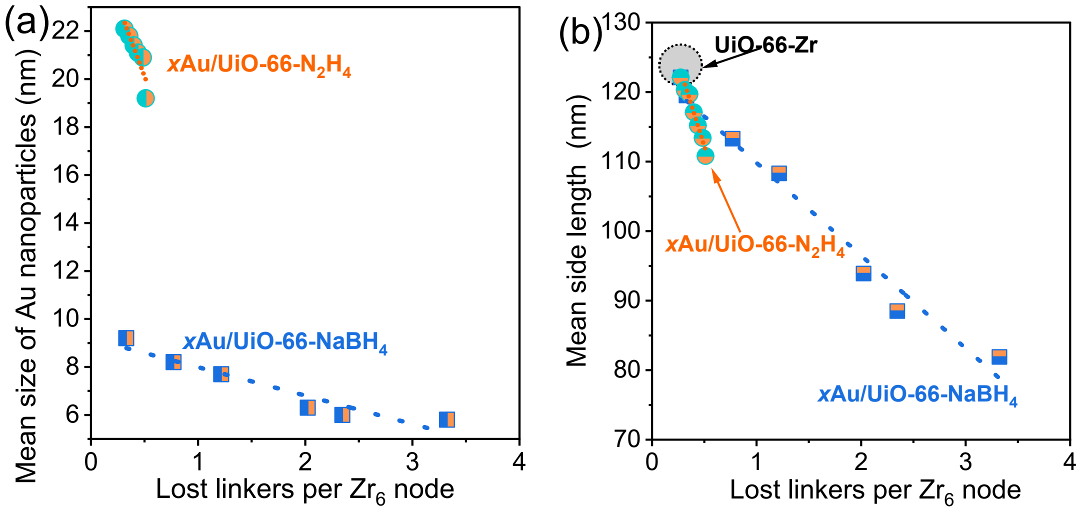

Fig. S14. (a) Relationship between lost linkers per Zr_6 node and mean sizes of Au nanoparticles; (b) Relationship between lost linkers per Zr_6 node and mean side lengths of octahedral UiO-66-Zr support nanoparticles.

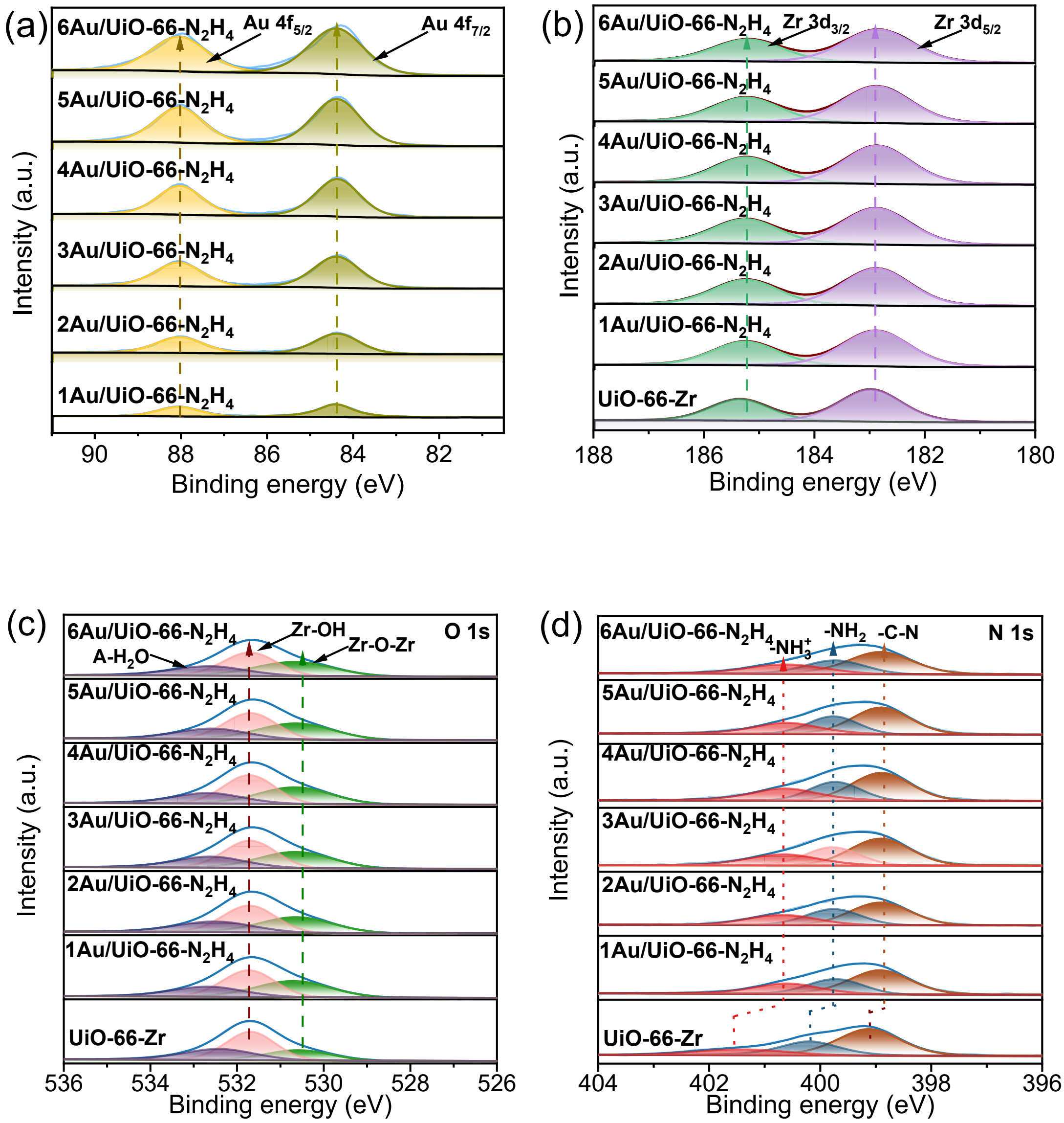

Fig. S15. XPS spectra of the pristine UiO-66-Zr and *x*Au/UiO-66-N$_2$H$_4$: (a) Au 4f; (b) Zr 3d; (c) O 1s; (d) N1s.

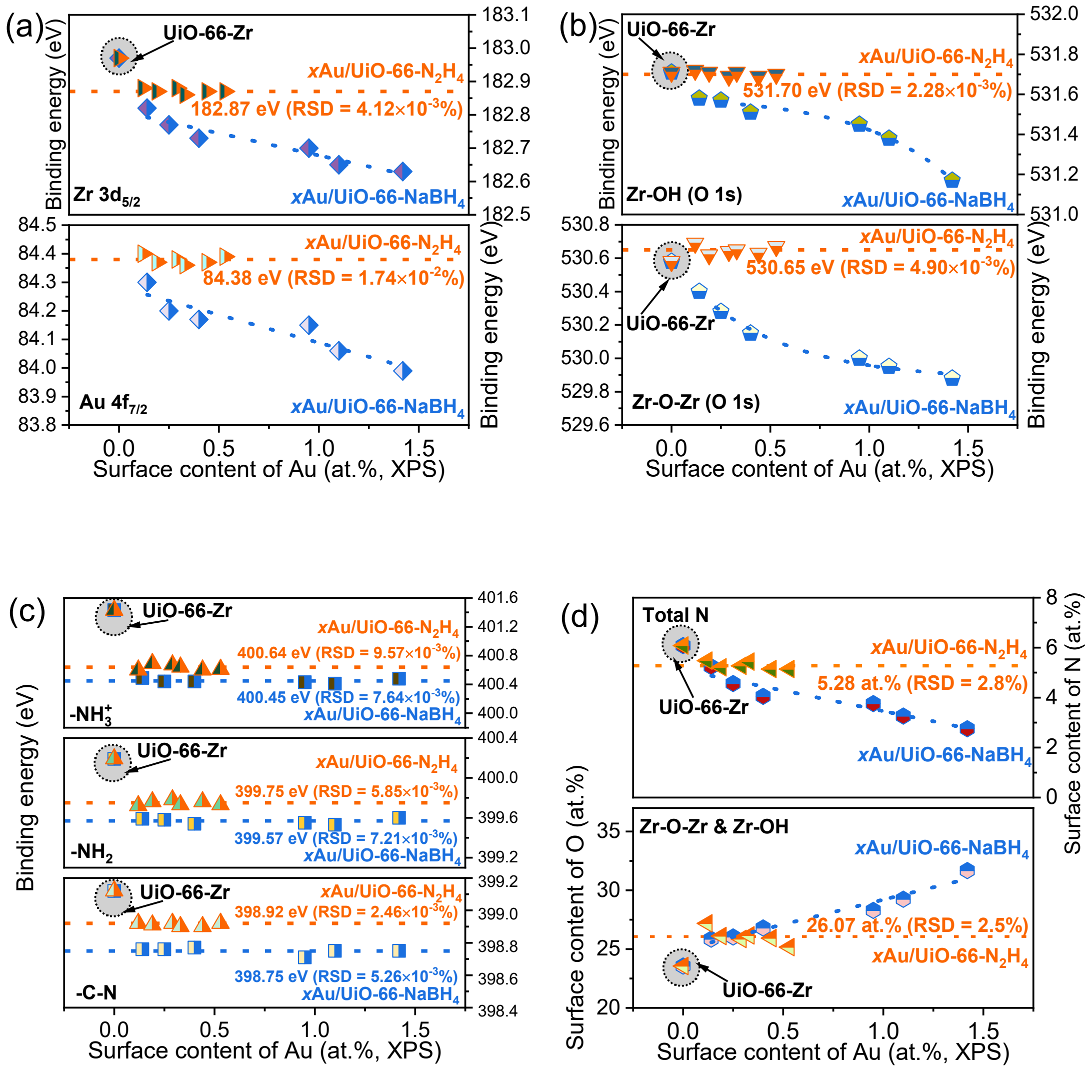

Fig. S16. (a) Relationship between surface contents of Au and *BE* values of Au $4f_{7/2}$ and Zr $3d_{5/2}$ (b) Relationship between surface contents of Au and *BE* values of Zr-O-Zr (O 1s) and Zr-OH (O 1s); (c) Relationship between surface contents of Au and *BE* values of -C-N, $-NH_2$ and $-NH_3^+$; (d) Relationship between surface contents of Au and those of Zr-O-Zr & Zr-OH and total N.

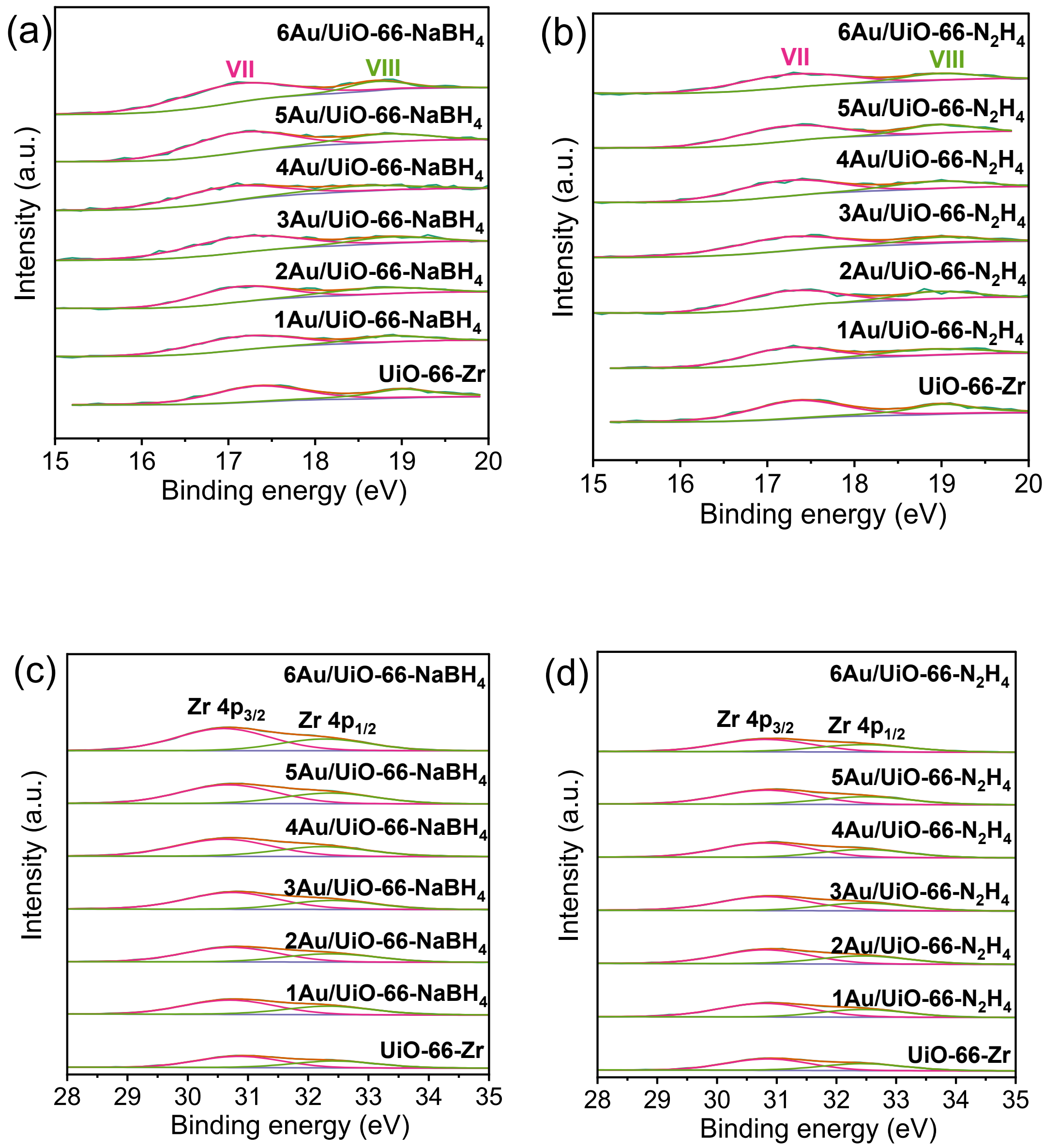

Fig. S17. Additional XPS VB spectra (15~20 eV and 28~35 eV) for the pristine UiO-66-Zr, *x*Au/UiO-66-$NaBH_4$ and *x*Au/UiO-66-N_2H_4.

Note S1: Bands VII and VIII within the range from 15 to 20 eV are attributed to C 2s and N 2s, respectively. The bands within the range from 28 to 35 eV correspond to Zr 4p, which also have spin-orbit doublets, i.e., Zr $4p_{3/2}$ and Zr $4p_{1/2}$. The *BE* values for C 2s for various samples of *x*Au/UiO-66-$NaBH_4$ are close, which have the mean value of

~17.12 eV with a low RSD of ~0.68%. Similar thing also happens to N 2s (mean value of ~18.78 eV with a low RSD of ~0.80%), Zr $4p_{3/2}$ (mean value of ~30.70 eV with a low RSD of ~0.28%), and Zr $4p_{1/2}$ (mean value of ~32.34 eV with a low RSD of ~0.21%). In addition, similar thing also happens to C 2s (mean value of ~17.24 eV with a low RSD of ~0.29%), N 2s (mean value of ~18.94 eV with a low RSD of ~0.23%), Zr $4p_{3/2}$ (mean value of ~30.82 eV with a low RSD of ~0.05%), and Zr $4p_{1/2}$ (mean value of ~32.46 eV with a low RSD of ~0.05%) for the samples of *x*Au/UiO-66-N_2H_4. The results suggest that the *BE* of C 2s, N 2s, and Zr 4p is hardly affected by the loaded Au or the lost-linker defects for both *x*Au/UiO-66-$NaBH_4$ and *x*Au/UiO-66-N_2H_4.

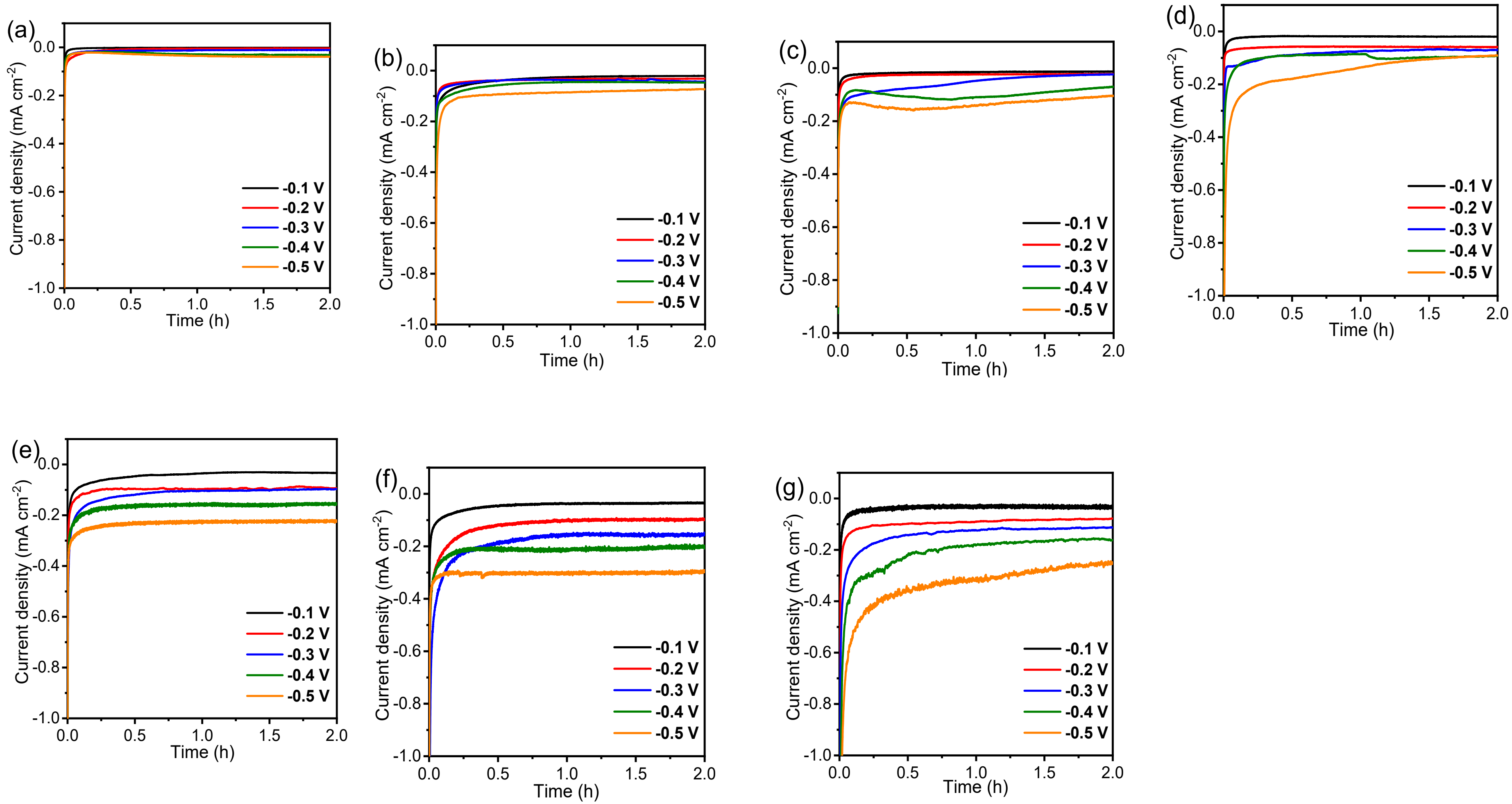
(a)
(b)
(c)
(d)
(e)
(f)
(g)
Current density (mA cm^{-2})
Time (h)
-0.1 V
-0.2 V
-0.3 V
-0.4 V
-0.5 V

Fig. S18. *I-t* curves at different potentials: (a) The pristine UiO-66-Zr; (b) 1Au/UiO-66-$NaBH_4$; (c) 2Au/UiO-66-$NaBH_4$, (d) 3Au/UiO-66-$NaBH_4$; (e) 4Au/UiO-66-$NaBH_4$; (f) 5Au/UiO-66-$NaBH_4$; (g) 6Au/UiO-66-$NaBH_4$.

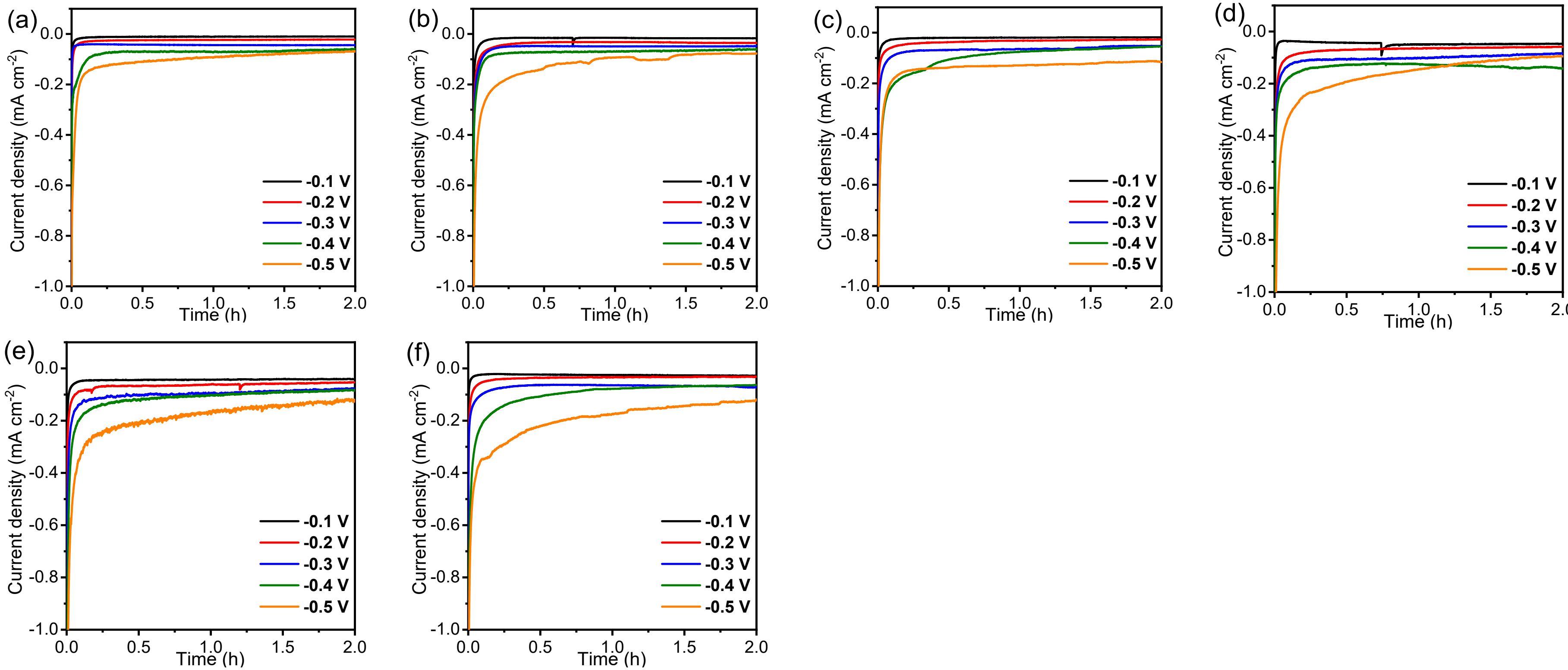

Fig. S19. *I-t* curves at different potentials: (a) 1Au/UiO-66-N_2H_4; (b) 2Au/UiO-66-N_2H_4; (c) 3Au/UiO-66-N_2H_4; (d) 4Au/UiO-66-N_2H_4; (e) 5Au/UiO-66-N_2H_4; (f) 6Au/UiO-66-N_2H_4.

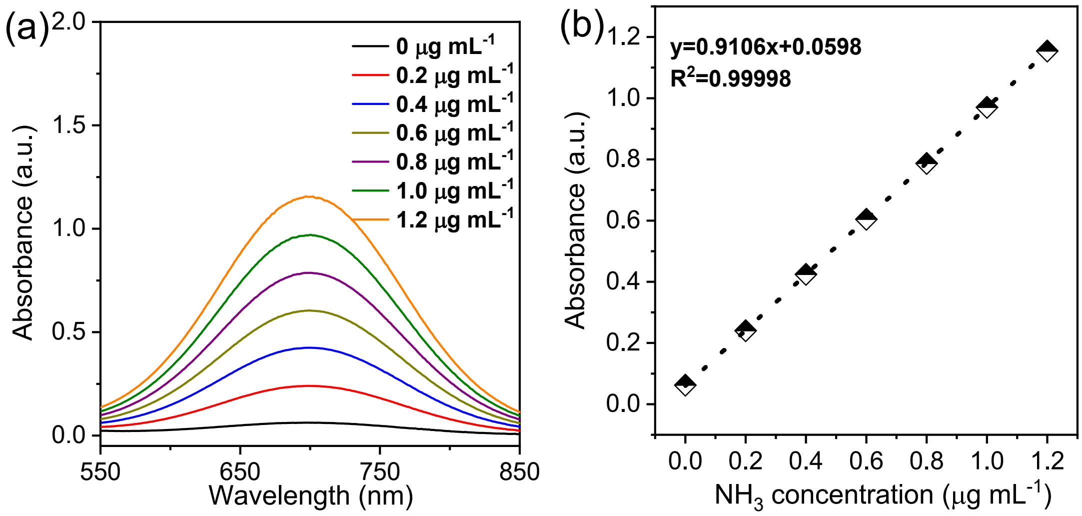

Fig. S20. (a) UV-vis spectra for ammonium chloride (NH_4Cl) solutions via indophenol method; (b) Standard absorbance-NH_3 concentration calibration curve.

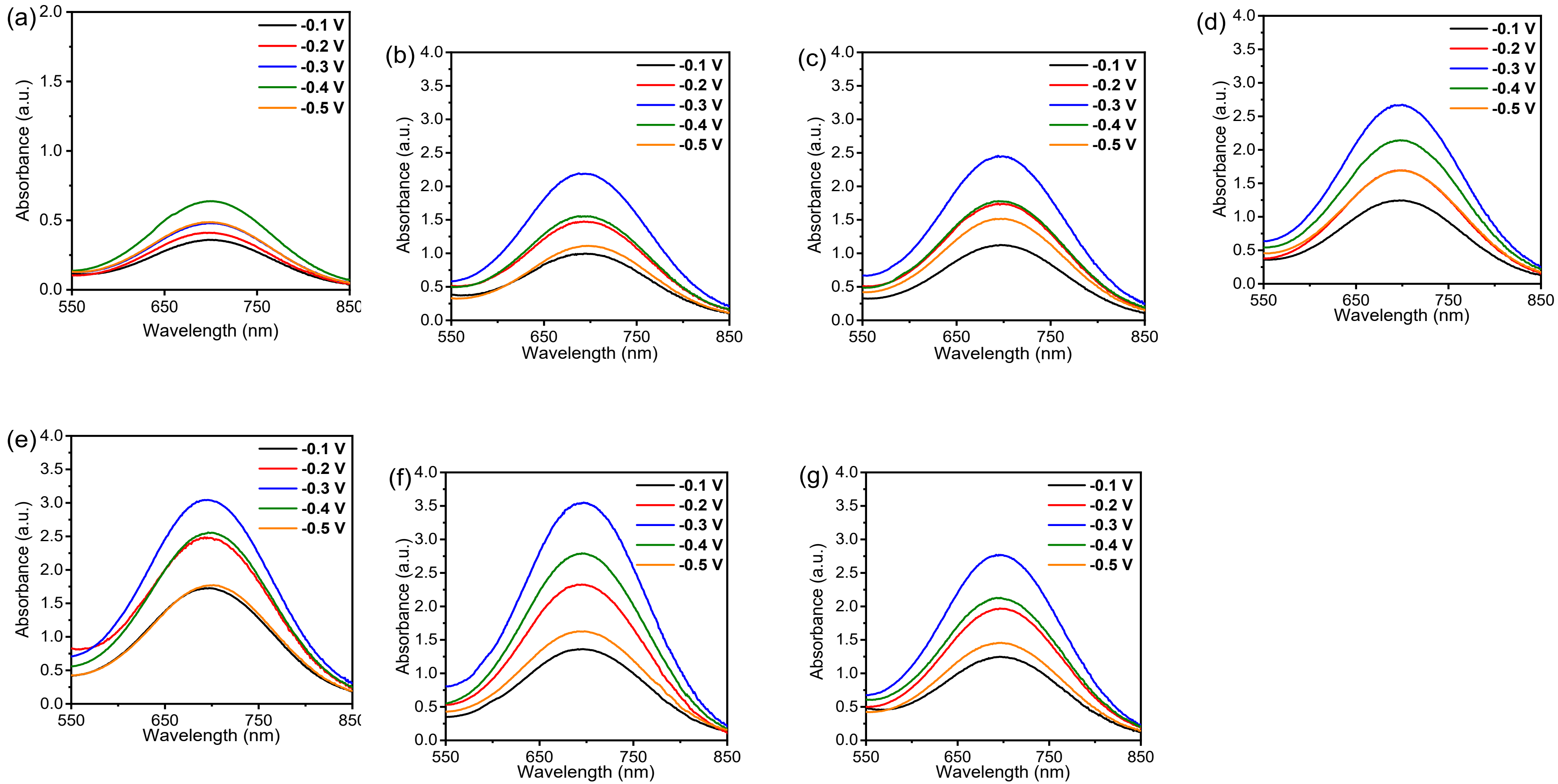
(a)
(b)
(c)
(d)
(e)
(f)
(g)
Absorbance (a.u.)
Wavelength (nm)
-0.1 V
-0.2 V
-0.3 V
-0.4 V
-0.5 V

Fig. S21. UV-vis absorption spectra using indophenol method under different potentials: (a) The pristine UiO-66-Zr; (b) 1Au/UiO-66-$NaBH_4$; (c) 2Au/UiO-66-$NaBH_4$, (d) 3Au/UiO-66-$NaBH_4$; (e) 4Au/UiO-66-$NaBH_4$; (f) 5Au/UiO-66-$NaBH_4$; (g) 6Au/UiO-66-$NaBH_4$.

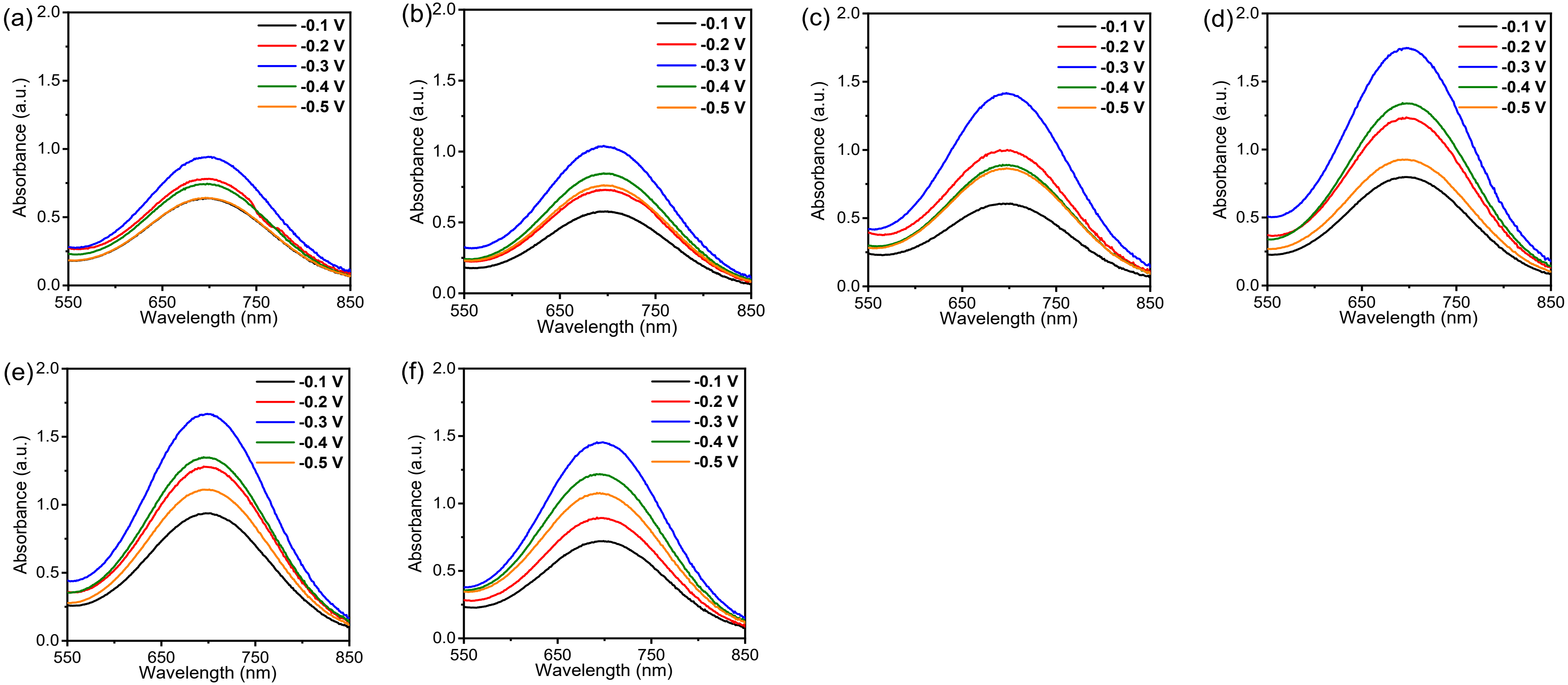

Fig. S22. UV-vis absorption spectra using indophenol method under different potentials: (a) 1Au/UiO-66-N_2H_4; (b) 2Au/UiO-66-N_2H_4; (c) 3Au/UiO-66-N_2H_4; (d) 4Au/UiO-66-N_2H_4; (e) 5Au/UiO-66-N_2H_4; (f) 6Au/UiO-66-N_2H_4.

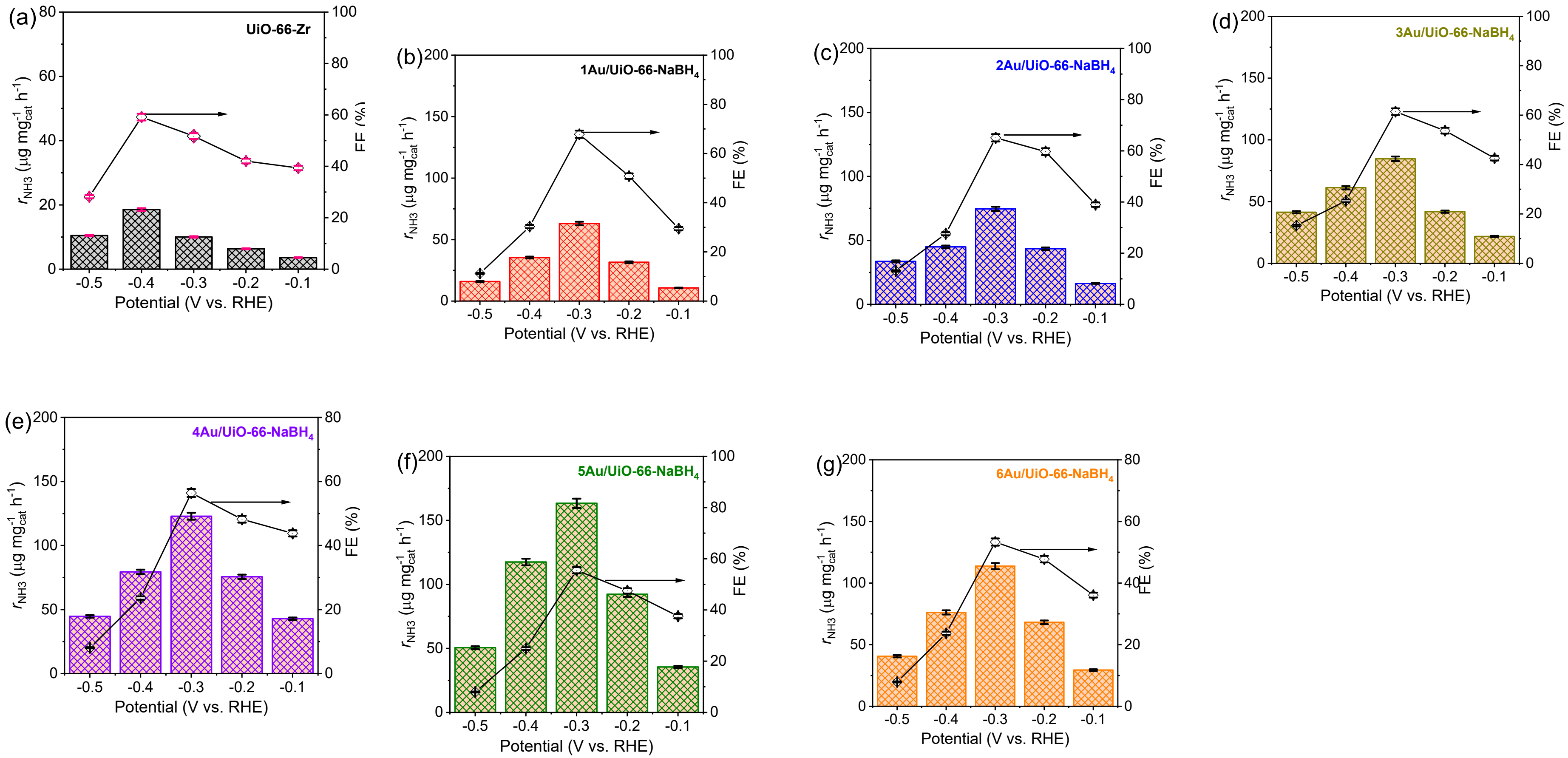

Fig. S23. R_{NH_3} **and FE at different potentials:** (a) The pristine UiO-66-Zr; (b) 1Au/UiO-66-NaBH$_4$; (c) 2Au/UiO-66-NaBH$_4$, (d) 3Au/UiO-66-

$NaBH_4$; (e) 4Au/UiO-66-$NaBH_4$; (f) 5Au/UiO-66-$NaBH_4$; (g) 6Au/UiO-66-$NaBH_4$.

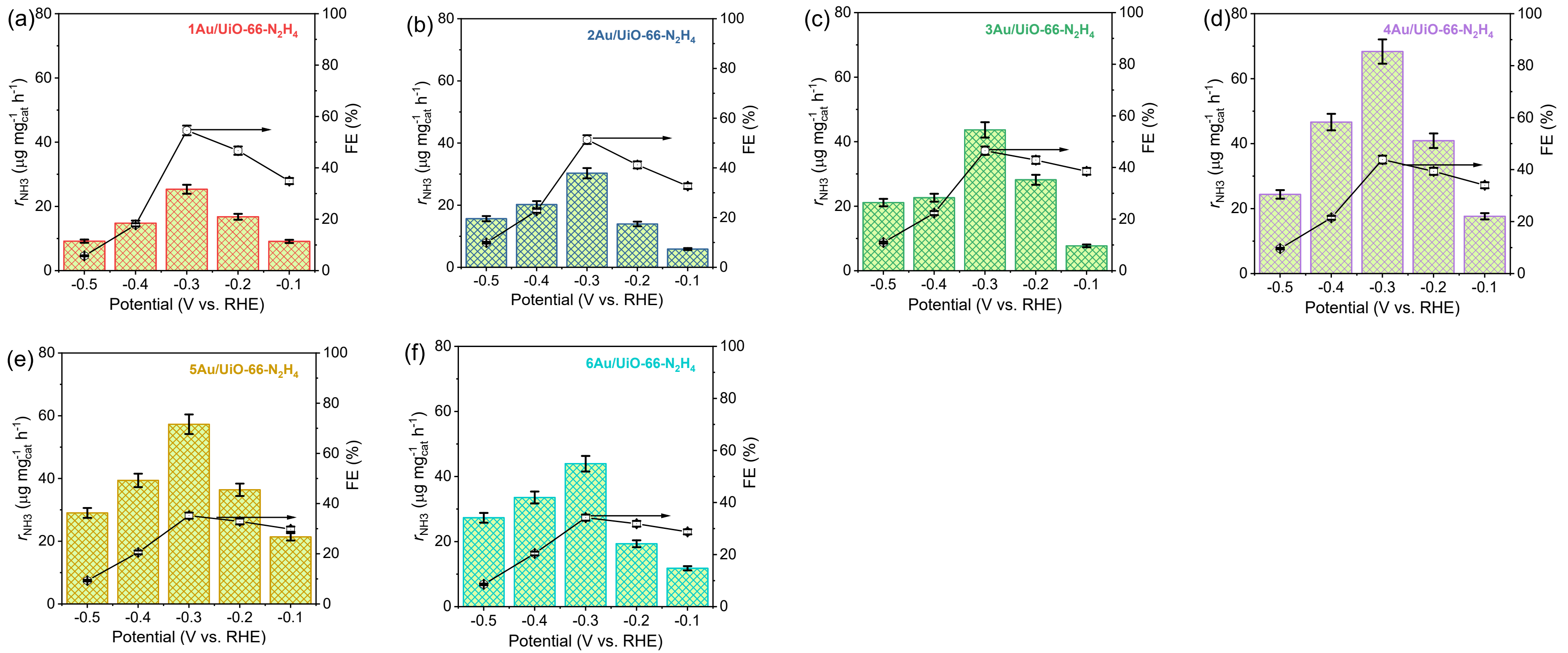

Fig. S24. R_{NH_3} **and FE at different potentials:** (a) 1Au/UiO-66-N_2H_4; (b) 2Au/UiO-66-N_2H_4; (c) 3Au/UiO-66-N_2H_4; (d) 4Au/UiO-66-N_2H_4; (e) 5Au/UiO-66-N_2H_4; (f) 6Au/UiO-66-N_2H_4.

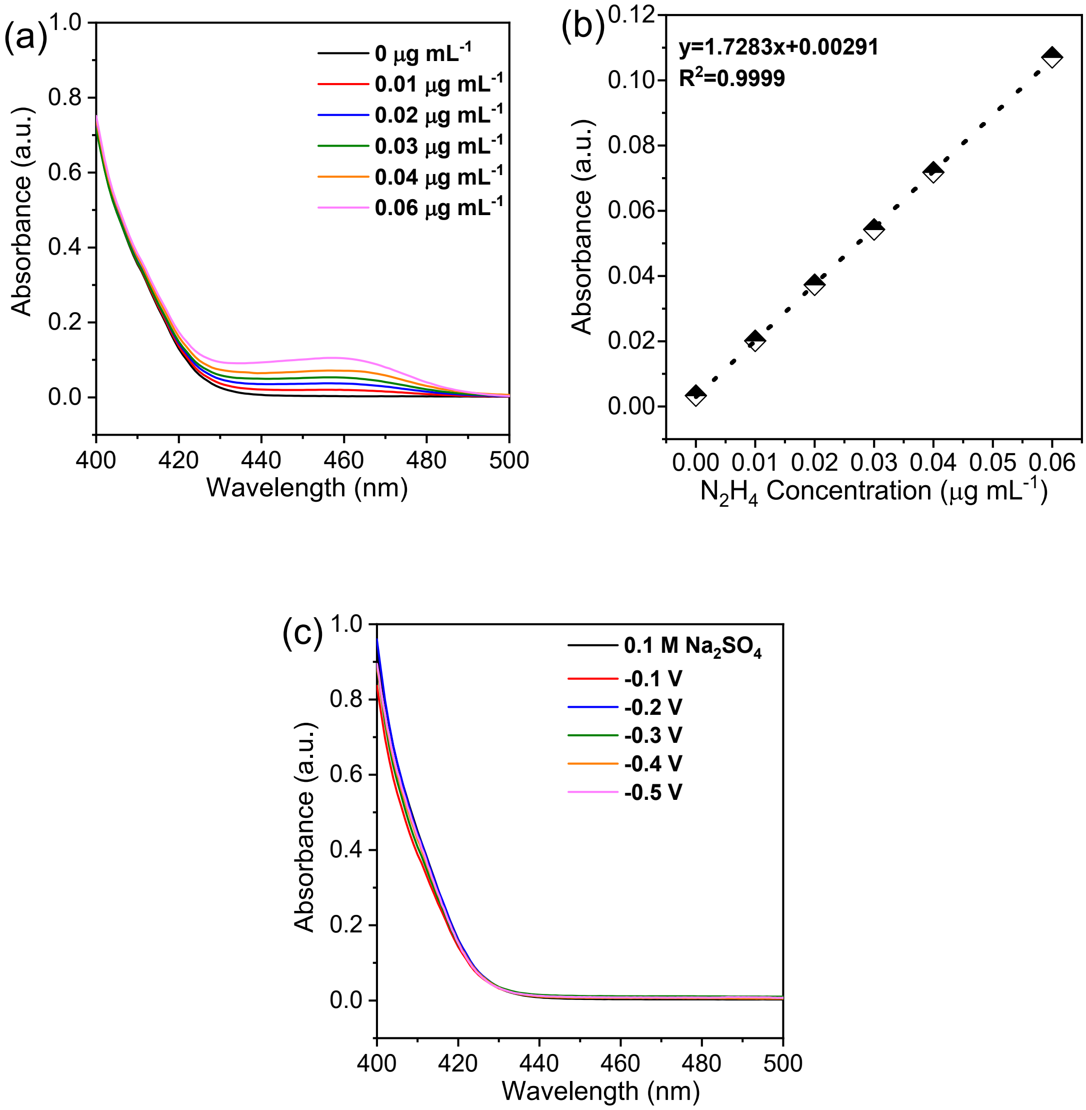

Fig. S25. (a) UV-vis spectra for standard N_2H_4 solutions via Watt-Chrisp method; (b) Absorbance-N_2H_4 concentration calibration curve; (c) UV-vis spectra of the electrolytes after NRR over 5Au/UiO-66-$NaBH_4$ via the Watt-Chrisp method.

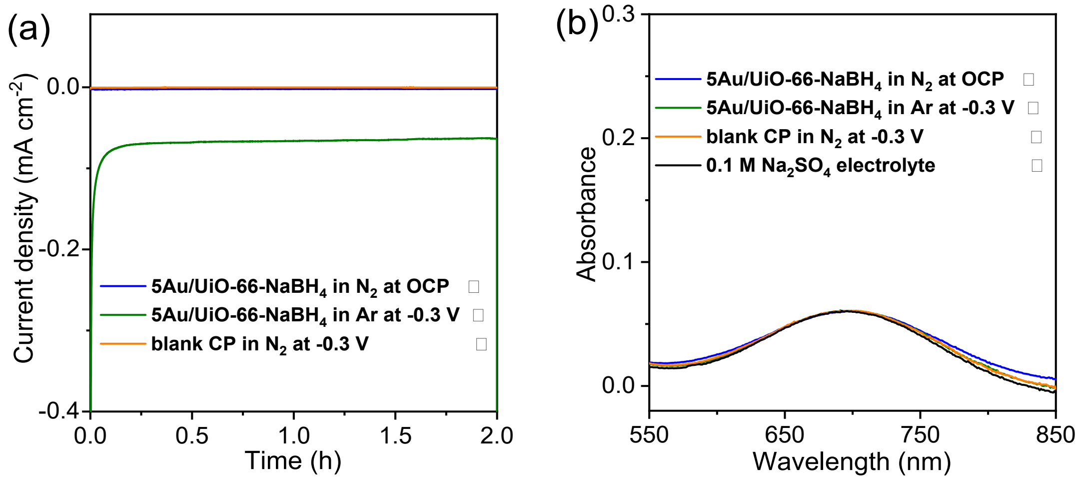

Fig. S26. (a) *I-t* curves of different control experiments; (b) UV-vis absorption spectra of the corresponding electrolytes.

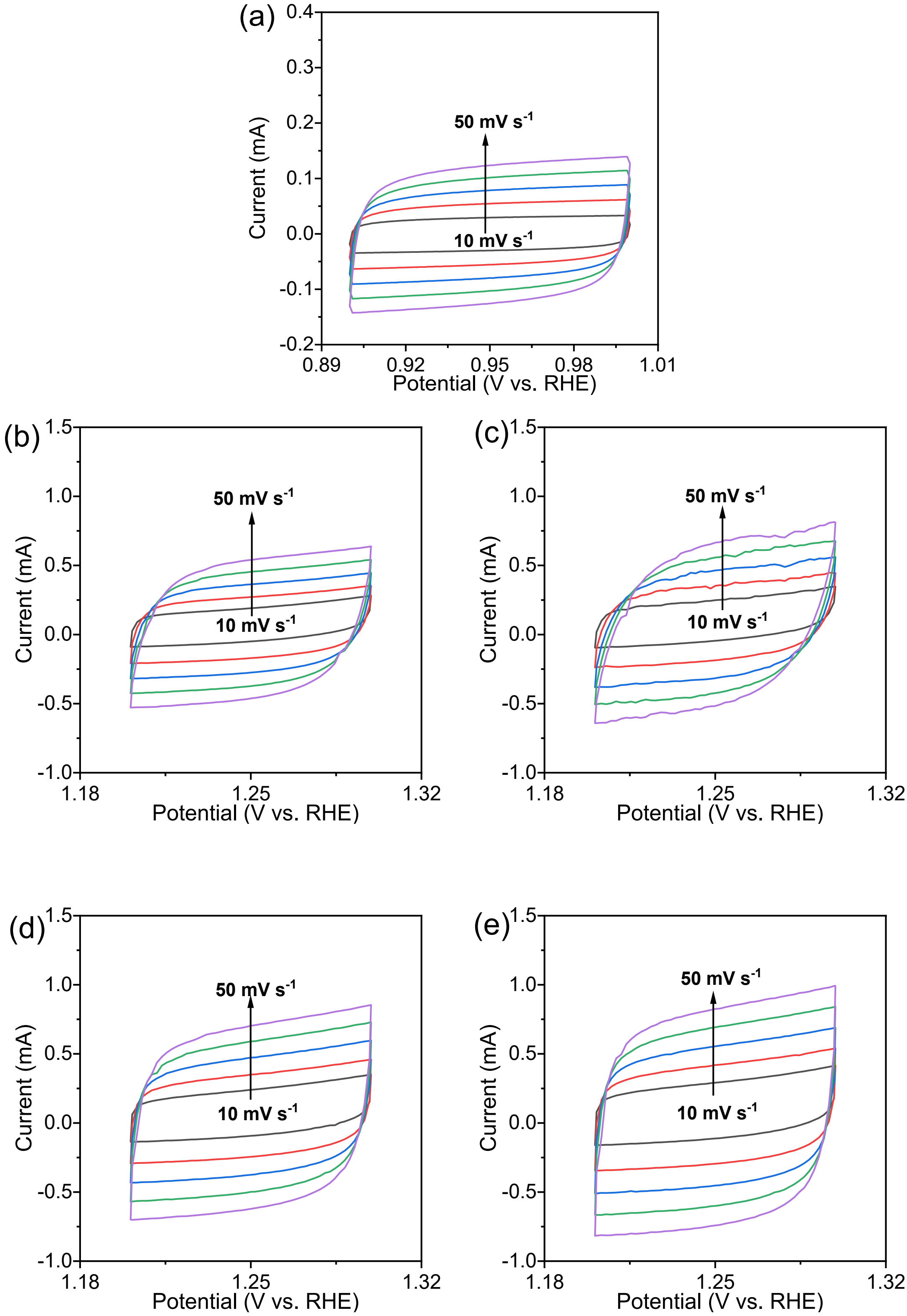

(a)
50 mV s-1
10 mV s-1
Current (mA)
Potential (V vs. RHE)
0.4
0.3
0.2
0.1
0.0
-0.1
-0.2
0.89
0.92
0.95
0.98
1.01
(b)
(c)
(d)
(e)
1.5
1.0
0.5
0.0
-0.5
-1.0
1.18
1.25
1.32

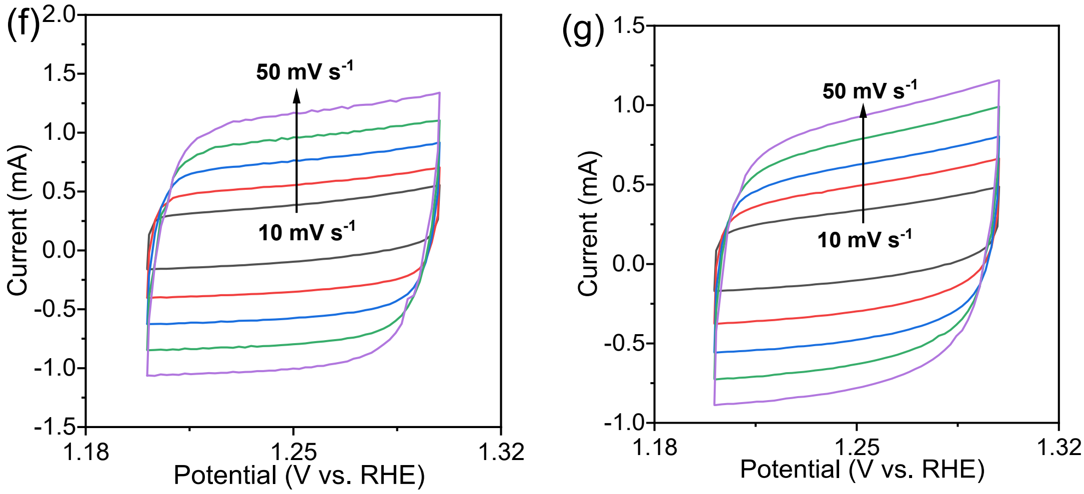

Fig. S27. CV curves at different scan rates within the potential ranges without Faradic currents: (a) The pristine UiO-66-Zr; (b) 1Au/UiO-66-NaBH_4; (c) 2Au/UiO-66-NaBH_4, (d) 3Au/UiO-66-NaBH_4; (e) 4Au/UiO-66-NaBH_4; (f) 5Au/UiO-66-NaBH_4; (g) 6Au/UiO-66-NaBH_4.

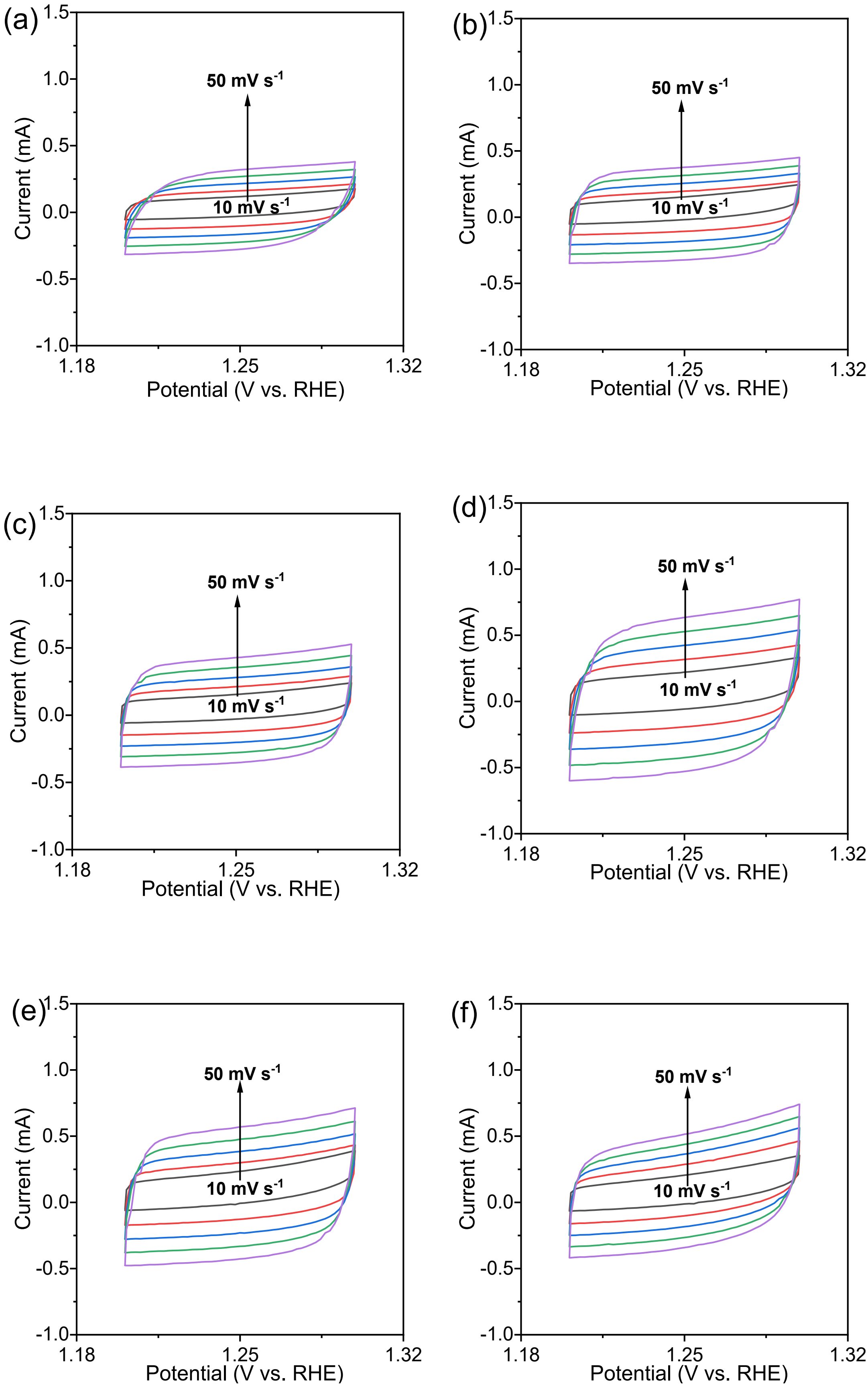
(a)
(b)
(c)
(d)
(e)
(f)
50 mV s-1
10 mV s-1
Current (mA)
Potential (V vs. RHE)
1.5
1.0
0.5
0.0
-0.5
-1.0
1.18
1.25
1.32

Fig. S28. CV curves at different scan rates within the potential ranges without Faradic currents: (a) 1Au/UiO-66-N_2H_4; (b) 2Au/UiO-66-N_2H_4; (c) 3Au/UiO-66-N_2H_4; (d) 4Au/UiO-66-N_2H_4; (e) 5Au/UiO-66-N_2H_4; (f) 6Au/UiO-66-N_2H_4.

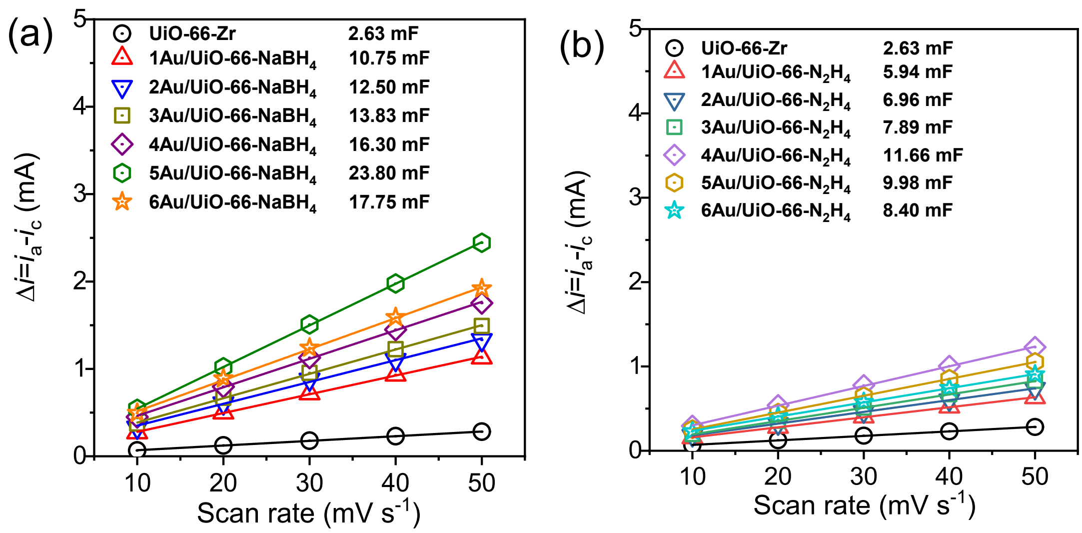

Fig. S29. (a) and (b) The plots of the relationship between scan rates and differences of anode and cathode currents for *x*Au/UiO-66-$NaBH_4$ and *x*Au/UiO-66-N_2H_4, respectively, also including that for the pristine UiO-66-Zr.

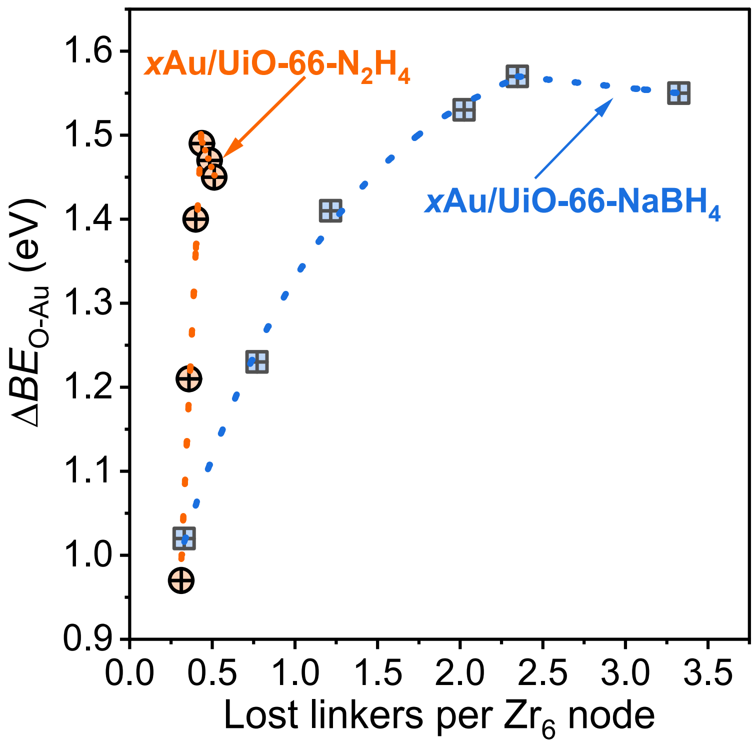

Fig. S30. Relations between $\Delta BE_{O\text{-}Au}$ and lost linkers per Zr_6 node.

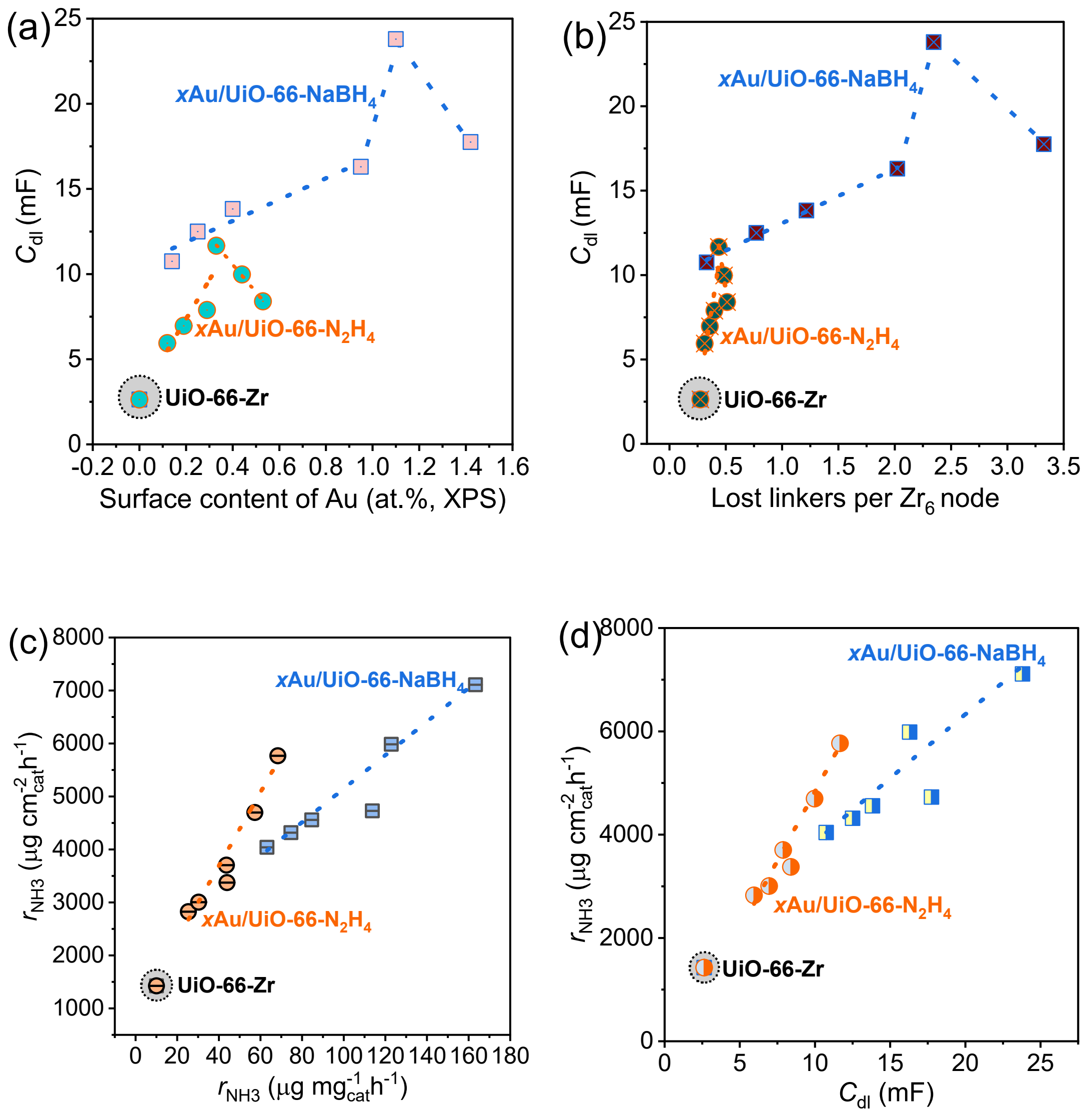

Fig. S31. (a) Relationships between surface contents of Au and C_{dl}; (b) Relationships between lost linkers per Zr_6 node and C_{dl}; (c) Relationships between r_{NH_3} and BET SSAs-normalized r_{NH_3}; (d) Relationships between C_{dl} and BET SSAs-normalized r_{NH_3}.

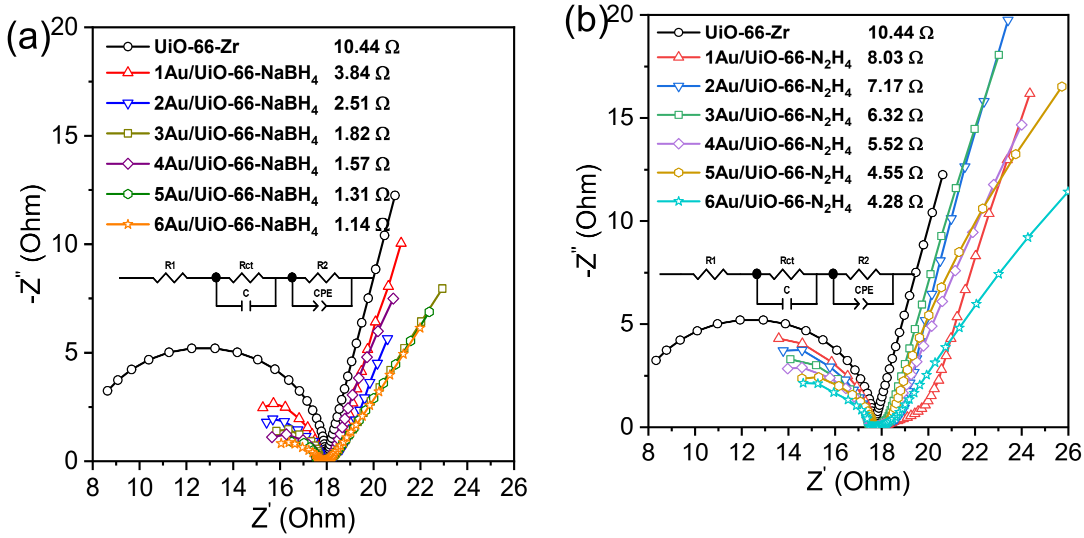

Fig. S32. (a) and (b) EIS plots at OCP for *x*Au/UiO-66-$NaBH_4$ and *x*Au/UiO-66-N_2H_4, respectively.

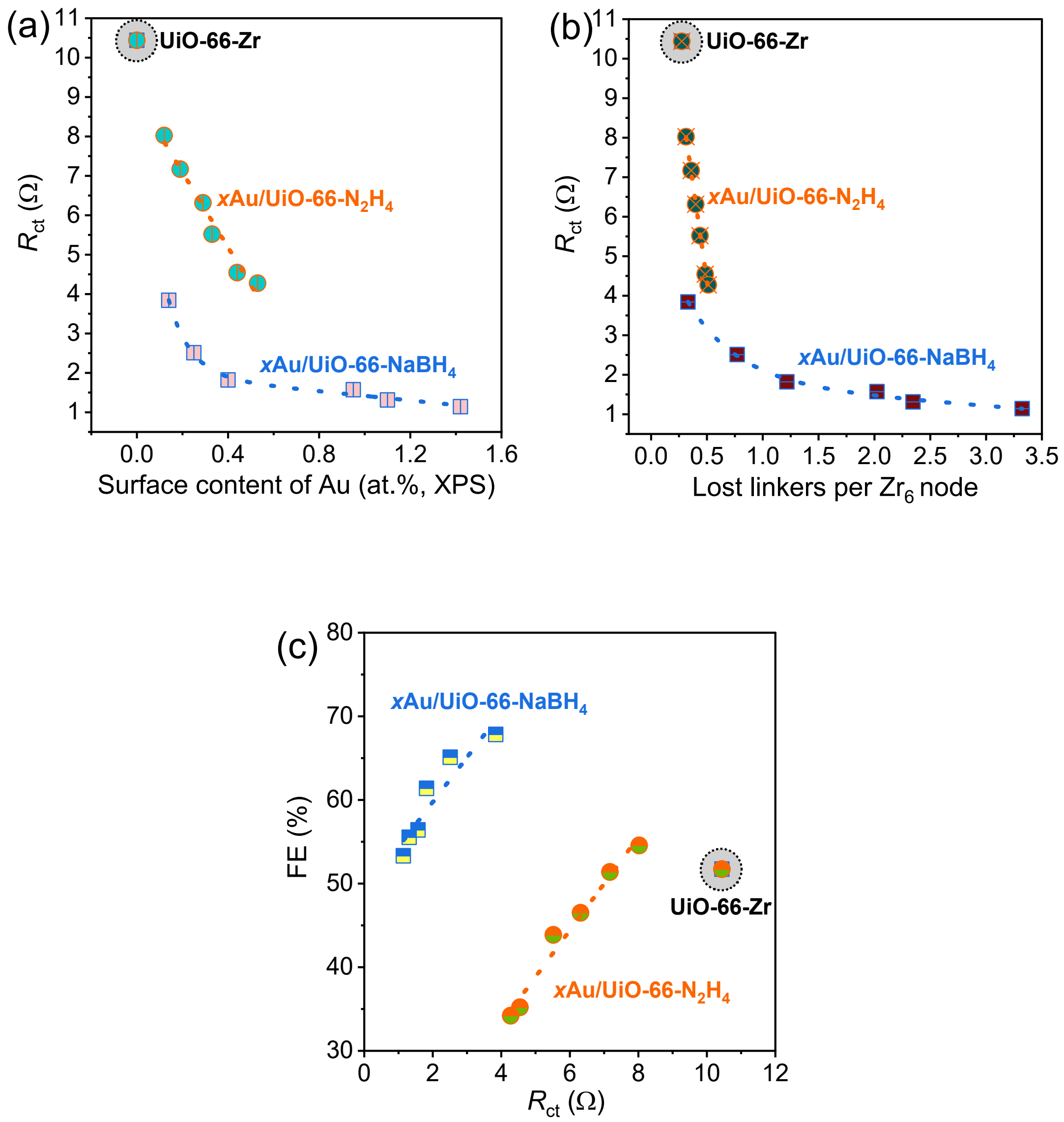

Fig. S33. (a) Relationships between surface contents of Au and R_{ct}; (b) Relationships between lost linkers per Zr_6 node and R_{ct}; (c) Relationships between R_{ct} and FE, and those between R_{ct} and r_{NH_3}.

Supporting Tables

Table S1. Core-level binding energy of surface species in the pristine UiO-66-Zr and *x*Au/UiO-66-NaBH$_4$.

Samples	N 1s (eV)			O 1s (eV)			Au 4f (eV)		$\Delta BE_{spin-orbit}$ (eV)	Zr 3d (eV)		$\Delta BE_{spin-orbit}$ (eV)
	-C-N	-NH$_2$	-NH$_3^+$	Zr-O-Zr	Zr-OH	A-H$_2$O	4f$_{7/2}$	4f$_{5/2}$		3d$_{5/2}$	3d$_{3/2}$	
The pristine UiO-66-Zr	399.12	400.19	401.43	530.58	531.71	532.55	-	-	-	182.97	185.34	2.37
1Au/UiO-66-NaBH$_4$	398.76	399.59	400.49	530.40	531.58	532.57	84.30	87.92	3.62	182.82	185.19	2.37
2Au/UiO-66-NaBH$_4$	398.76	399.58	400.44	530.28	531.57	532.37	84.20	87.85	3.65	182.77	185.14	2.37
3Au/UiO-66-NaBH$_4$	398.77	399.54	400.44	530.15	531.51	532.22	84.17	87.83	3.66	182.73	185.10	2.37

4Au/UiO-66-NaBH$_4$	398.71	399.55	400.43	530.00	531.45	532.34	84.15	87.81	3.66	182.70	185.07	2.37
5Au/UiO-66-NaBH$_4$	398.75	399.53	400.41	529.95	531.38	532.40	84.06	87.71	3.65	182.65	185.01	2.36
6Au/UiO-66-NaBH$_4$	398.75	399.6	400.48	529.88	531.17	532.16	83.99	87.64	3.65	182.63	185.00	2.37

Table S2. Core-level binding energy of surface species in *x*Au/UiO-66-N_2H_4.

Samples	N 1s (eV)			O 1s (eV)			Au 4f (eV)		$\Delta BE_{spin\text{-}orbit}$ (eV)	Zr 3d (eV)		$\Delta BE_{spin\text{-}orbit}$ (eV)
	-C-N	$-NH_2$	$-NH_3^+$	Zr-O-Zr	Zr-OH	A-H_2O	$4f_{7/2}$	$4f_{5/2}$		$3d_{5/2}$	$3d_{3/2}$	
1Au/UiO-66-N_2H_4	398.92	399.72	400.60	530.69	531.72	532.68	84.40	88.04	3.64	182.88	185.25	2.37
2Au/UiO-66-N_2H_4	398.91	399.76	400.69	530.62	531.71	532.50	84.37	88.02	3.65	182.87	185.24	2.37
3Au/UiO-66-N_2H_4	398.92	399.78	400.67	530.64	531.69	532.61	84.38	88.04	3.66	182.88	185.25	2.37
4Au/UiO-66-N_2H_4	398.90	399.73	400.64	530.65	531.71	532.66	84.36	88.02	3.66	182.86	185.23	2.37
5Au/UiO-66-	398.90	399.76	400.60	530.63	531.69	532.58	84.37	88.03	3.66	182.87	185.23	2.36

N_2H_4											
6Au/UiO-66-N_2H_4	398.92	399.73	400.61	530.67	531.70	532.64	84.39	88.04	3.65	182.87	185.24	2.37

Table S3. Surface atomic compositions of the pristine UiO-66-Zr and *x*Au/UiO-66-$NaBH_4$ determined by XPS.

Samples	N (at%)				O (at%)					Au (at%)	Zr (at%)
	-C-N	$-NH_2$	$-NH_3^+$	Total	Zr-O-Zr	Zr-OH	A-H_2O [a)]	Zr-O-Zr & Zr-OH	Total		
The pristine UiO-66-Zr	3.40	1.76	0.91	6.08	7.91	15.65	7.90	23.56	31.46	-	4.27
1Au/UiO-66-$NaBH_4$	2.53	1.54	1.17	5.24	10.21	15.64	8.75	25.85	34.60	0.14	5.25
2Au/UiO-66-$NaBH_4$	2.02	1.50	1.04	4.56	9.41	16.62	9.05	26.03	35.08	0.25	5.39
3Au/UiO-66-$NaBH_4$	1.92	1.17	0.96	4.05	9.12	17.68	9.23	26.80	36.03	0.40	5.73
4Au/UiO-66-$NaBH_4$	1.71	0.92	1.13	3.76	8.89	19.4	9.67	28.29	37.96	0.95	6.64
5Au/UiO-66-$NaBH_4$	1.32	0.87	1.07	3.26	8.01	21.23	10.75	29.24	39.99	1.10	7.16
6Au/UiO-66-$NaBH_4$	1.00	0.73	1.02	2.75	7.78	23.90	12.99	31.68	44.67	1.42	8.14

[a)] A-H_2O refers to adsorbed H_2O.

Table S4. Surface atomic compositions of *x*Au/UiO-66-N_2H_4 determined by XPS.

Samples	N (at%) [a]				O (at%) [a]					Au (at%)	Zr (at%) [a]
	-C-N	$-NH_2$	$-NH_3^+$	Total	Zr-O-Zr	Zr-OH	A-H_2O	Zr-O-Zr & Zr-OH	Total		
1Au/UiO-66-N_2H_4	2.79	1.39	1.30	5.48	12.73	14.46	7.99	27.19	35.18	**0.12**	5.16
2Au/UiO-66-N_2H_4	2.47	1.53	1.22	5.21	11.89	14.22	8.52	26.11	34.63	**0.19**	5.20
3Au/UiO-66-N_2H_4	2.53	1.45	1.29	5.27	11.96	13.9	8.43	25.86	34.29	**0.29**	5.06
4Au/UiO-66-N_2H_4	2.55	1.40	1.49	5.44	11.97	14.19	7.86	26.16	34.02	**0.33**	5.15
5Au/UiO-66-N_2H_4	2.51	1.32	1.31	5.14	12.35	13.58	7.8	25.93	33.73	**0.44**	5.16
6Au/UiO-66-N_2H_4	2.65	1.33	1.16	5.14	11.88	13.29	8.29	25.17	33.46	**0.53**	5.04

[a] The mean surface contents of -C-N, $-NH_2$, $-NH_3^+$, total N, Zr-O-Zr, Zr-OH, A-H_2O (referred to adsorbed H_2O), Zr-O-Zr & Zr-OH, total O and Zr are ~2.58, ~1.41, ~1.29, ~5.28, ~12.13, ~13.94, ~8.15, ~26.07, ~34.22 and ~5.13 at%, respectively, and the corresponding RSD values are ~4.6, ~5.5, ~8.6, ~2.8, ~2.8, ~3.2, ~3.8, ~2.5, ~1.8% and ~1.2%, respectively. But, the changes of the surface contents of Au are more significant (mean:

~0.32 at%, RSD: ~48%).

Table S5. XPS valence band binding energy (-4.5~15 eV) in the pristine UiO-66-Zr, *x*Au/UiO-66-$NaBH_4$ and *x*Au/UiO-66-N_2H_4.

Samples	Au $5d_{5/2}$ (eV)	Au $5d_{3/2}$ (eV)	$\Delta BE_{spin\text{-}orbit}$ (Au $5d_{3/2}$- Au $5d_{5/2}$, eV)	$\Delta BE_{O\text{-}Au}$ (O 2p non-bonding-Au $5d_{5/2}$, eV)	O 2p non-bonding (eV)	O 2p bonding (eV)	C 2p (3e2g+1a2u, eV)	C 2p (3e1u+1b2u, eV)
The pristine UiO-66-Zr	--	--	--	--	4.73	6.86	10.14	12.98
1Au/UiO-66-$NaBH_4$	3.71	6.12	2.41	1.02	4.73	7.39	10.05	12.75
2Au/UiO-66-$NaBH_4$	3.5	6.15	2.65	1.23	4.73	7.38	10.1	12.63
3Au/UiO-66-$NaBH_4$	3.25	6.1	2.85	1.41	4.66	7.35	10.07	12.74
4Au/UiO-66-	3.04	6.14	3.1	1.53	4.57	7.31	10.06	12.55

$NaBH_4$								
5Au/UiO-66-$NaBH_4$	2.83	5.99	3.16	1.57	4.4	7.2	10.03	12.53
6Au/UiO-66-$NaBH_4$	2.75	5.96	3.21	1.55	4.3	7.23	9.75	12.49
1Au/UiO-66-N_2H_4	3.77	6.04	2.27	0.97	4.74	7.38	10.17	12.98
2Au/UiO-66-N_2H_4	3.55	6.09	2.54	1.21	4.76	7.39	10.12	12.90
3Au/UiO-66-N_2H_4	3.33	6.11	2.78	1.40	4.73	7.39	10.25	12.88
4Au/UiO-66-N_2H_4	3.26	6.14	2.88	1.49	4.75	7.3	10.11	12.8

5Au/UiO-66-N_2H_4	3.19	6.13	2.94	1.47	4.66	7.44	10.21	12.69
6Au/UiO-66-N_2H_4	3.19	6.03	2.84	1.45	4.64	7.34	10.08	12.86

Table S6. Summary of the recently-developed catalysts toward NRR to NH_3.

Catalyst	r_{NH_3} ($\mu g\ h^{-1}\ mg_{cat}^{-1}$)	FE (%)	Electrolyte	Potential (V vs. RHE)	Loading ($mg\ cm^{-2}$)	Refs.
5Au/UiO-66-$NaBH_4$	**163.33**	**55.52**	**0.1 M Na_2SO_4**	**-0.3**	**0.5**	**This work**
HT Au@MOF	49.5	60.9	0.1 M Na_2SO_4	-0.3	N.A.	[1]
Ru SAs/N-C	120.9	29.6	0.05 M H_2SO_4	-0.2	0.255	[2]
Ru SAs/g-C_3N_4	23	8.3	0.5 M NaOH	0.05	N.A.	[3]
Rh@SnO_2	149	11.69	0.05 M H_2SO_4	-0.35	0.05	[4]
OVs-Pd_3Pb-2	88.3	41.1	0.1 M Li_2SO_4	-0.05	N.A.	[5]
Fe_2O_3@MoS_2	112.15	8.62	0.1 M Na_2SO_4	-0.6 for r_{NH_3} -0.4 for FE	0.3	[6]
C@YSZ	24.60	8.2	0.1 M Na_2SO_4	-0.5	0.2	[7]

Ni-Fe@MoS_2	128.17	11.34	0.1 M Na_2SO_4 (@40 ^{o}C)	-0.3	0.71	[8]
C-BN	44.59	13.27	0.1 M Na_2SO_4	-0.9 for r_{NH_3} -0.7 for FE	0.24	[9]
Zn^1N-C	16.1	11.8	0.1 M KOH	-0.3	N.A.	[10]
Bi@C	4.22	15.1	0.1 M Na_2SO_4	-0.6 for r_{NH_3} -0.4 for FE	0.25	[11]
NC/Bi SAs/TiN/CC	76.15	24.6	0.1 M Na_2SO_4	-0.8 for r_{NH_3} -0.5 for FE	N.A.	[12]
Rh_2P@NPC	37.5	7.64	0.05 M H_2SO_4	-0.25 for r_{NH_3} -0.05 for FE	0.2	[13]
FeMoPPc	36.33	20.62	0.1 M KOH	-0.3	0.5	[14]

Supporting references

1 H.M. He, Q.Q. Zhu, Y. Yan, H.W. Zhang, Z.Y. Han, H.M. Sun, J. Chen, C.P. Li, Z.H. Zhang and M. Du, Metal-organic framework supported Au nanoparticles with organosilicone coating for high-efficiency electrocatalytic N_2 reduction to NH_3, *Appl. Catal. B*, 2022, **302**, 120840.

2 Z. Geng, Y. Liu, X. Kong, P. Li, K. Li, Z. Liu, J. Du, M. Shu, R. Si and J. Zeng, Achieving a record-high yield rate of 120.9$\mu g_{NH_3} mg_{cat.}^{-1} h^{-1}$ for N_2 electrochemical reduction over Ru single-atom catalysts, *Adv. Mater.*, 2018, **30**, 1803498.

3 B. Yu, H. Li, J. White, S. Donne, J.B. Yi, S. Xi, Y. Fu, G. Henkelman, H. Yu, Z.L. Chen and T.Y. Ma, Tuning the catalytic preference of ruthenium catalysts for nitrogen reduction by atomic dispersion, *Adv. Funct. Mater.*, 2020, **30**, 1905665.

4 Y.Q. Liu, L. Huang, Y.X. Fang, X.Y. Zhu, J.L. Nan and S.J. Dong, Interfacial electron regulation of Rh atomic layer-decorated SnO_2 heterostructures for enhancing electrocatalytic nitrogen reduction, *ACS Appl. Mater. Interfaces*, 2022,**14**, 12304-12313.

5 Z.C. Wang, J. Liu, X.K. Wu, N.Z. Nie, D. Zhang, H.D. Li, H. Zhao, J.P. Lai and L. Wang, Engineering ordered vacancies and atomic arrangement over the intermetallic PdM/CNT (M=Pb,Sn,In) nanocatalysts for synergistically promoting electrocatalysis N_2 fixation, *Appl. Catal. B*, 2022, **314**, 121465.

6 C.Q. Ma, D. Liu, Y.L. Zhang, J.Y. Lee, J. Tian, B.P. Liu and S.H. Yan, MOF-derived Fe_2O_3@MoS_2: An efficient electrocatalyst for ammonia synthesis under mild conditions, *Chem. Eng. J.*, 2022, **430**, 132694.

7 S.J. Luo, X.M. Li, M.Y. Wang, X. Zhang, W.G. Gao, S.D Su, G.W. Liu and M. Luo, Long-term electrocatalytic N_2 fixation by MOF-derived Y-stabilized ZrO_2: insight into the deactivation mechanism, *J. Mater. Chem. A*, 2020, **8**, 5647-5654.

8 L.B. Zeng, X.Y. Li, S. Chen, J.L. Wen, W. Huang and A. Chen, Unique hollow Ni-Fe@MoS_2 nanocubes with boosted electrocatalytic activity for N_2 reduction to NH_3, *J. Mater. Chem. A*, 2020, **8**, 7339-7349.

9 C.Q. Ma, Y.L. Zhang, S.H. Yan and B.P. Liu, Carbon-doped boron nitride nanosheets: A high-efficient electrocatalyst for ambient nitrogen reduction, *Appl. Catal. B*, 2022, **315**, 121574.

10 Y. Kong, Y. Li, X.H. Sang, B. Yang, Z.J. Li, S.X. Zheng, Q.H. Zhang, S.Y. Yao, X.X. Yang, L.C. Lei, S.D. Zhou, G. Wu and Y. Hou, Atomically dispersed zinc(I) active sites to accelerate nitrogen reduction kinetics for ammonia electrosynthesis, *Adv. Mater*., 2022, **34**, 2103548.

11 Y.C. Wan, H.J. Zhou, M.Y. Zheng, Z.H. Huang, F.Y. Kang, J. Li and R.T. Lv, Oxidation state modulation of bismuth for efficient electrocatalytic nitrogen reduction to ammonia, *Adv. Funct. Mater*., 2021, **31**, 2100300.

12 Z.C. Xi, K. Shi, X. Xu, P. Jing, B.C. Liu, R. Gao and J. Zhang, Boosting nitrogen reduction reaction via electronic coupling of atomically dispersed bismuth with titanium nitride nanorods, *Adv. Sci*., 2022, **9**, 2104245.

13 J.F. Su, H.Y. Zhao, W.W. Fu, W. Tian, X.H. Yang, H.J. Zhang, F.L. Ling and Y. Wang, Fine rhodium phosphides nanoparticles embedded in N, P dual-doped carbon film: New efficient electrocatalysts for ambient nitrogen fixation, *Appl.*

Catal. B, 2020, **265**, 118589.

14 Y.J. Wang, W.Z. Cheng, P.F. Yuan, G.G. Yang, S.C. Mu, J.L. Liang, H.C. Xia, K. Guo, M.L. Liu, S.Y. Zhao, G. Qu, B.A. Lu, Y.F. Hu, J.S. Hu and J.N. Zhang, Boosting nitrogen reduction to ammonia on FeN_4 sites by atomic spin regulation, *Adv. Sci*., 2021, **8**, 2102915.